A Progressive Inversion Scheme for Three-dimensional Imaging of Seismic Velocities in Earth's Mantle

By

R. Jay Pulliam
Department of Statistics
University of California, Berkeley

Lane R. Johnson
Department of Geology and Geophysics
University of California, Berkeley

both authors are also at the
Center for Computational Seismology
Lawrence Berkeley Laboratory
Berkeley, California

Technical Report No. 360
July 1992

Department of Statistics
University of California
Berkeley, California 94720

A Progressive Inversion Scheme for Three-dimensional Imaging of Seismic Velocities in Earth's Mantle

R. JAY PULLIAM

Department of Statistics
University of California, Berkeley

LANE R. JOHNSON

Department of Geology and Geophysics
University of California, Berkeley

both authors are also at the

Center for Computational Seismology
Lawrence Berkeley Laboratory
Berkeley, California

ABSTRACT

We investigate the effects of mislocated earthquakes on the velocity model obtained in tomographic inversions for mantle structure and the ability of simultaneous and progressive inversion techniques to correct earthquake mislocations and produce an accurate velocity model. We solve a system of tomographic travel time equations in three ways: (a) directly, neglecting source terms, (b) simultaneously for both velocity model terms and corrections to the source locations, and (c) progressively, for each set of terms in succession. The algorithms all perform least-squares inversions; they differ primarily in their treatment of source mislocation terms.

Simulations demonstrate that ignoring the effects of source mislocation results in underestimating velocity anomalies by up to 50%, creates smeared anomalies in adjacent voxels with values up to 50% of the retrieved velocity of its neighbor, and creates anomalies elsewhere in the mantle with values greater than those estimated for input anomalies. Clearly, careful treatment of the source location problem is critical to the accurate estimation of three-dimensional velocity variations. The progressive inversion developed here generally produces more accurate source corrections and velocity anomaly estimates than does an inversion scheme in which both source corrections and velocity terms are found simultaneously. These results are superior particularly with respect to the suppression of artificial anomalies.

Electronic mail: pulliam@stat.berkeley.edu, lrj@geo.lbl.gov

We also apply these algorithms to real data supplied by the ISC. We use P arrival data from January 1964 through January 1987 to solve for three-dimensional P velocity models of the mantle and source mislocations. The model mantle is parametrized by approximately equal-area blocks: 10° × 10° and generally 200 km in depth. Nearly 345,000 rays from more than 3,000 shallow events satisfying selection criteria are included in the inversions. A comparison of the models found by neglecting source terms, by solving simultaneously for source and velocity terms, and by solving progressively reveals that upper mantle differences are located primarily in source regions, implying that the model differences result from the differences in our treatment of the source terms. Despite the concentration of model differences in source regions, the effects of different treatments of the source appear in the velocity models at both long and short wavelengths in the upper mantle. Differences between the models diminish with depth. A comparison of the source corrections produced by simultaneous and progressive inversion supports the interpretation that model differences are concentrated in source regions. Source corrections emerging from the progressive inversion are generally two to four times greater than the simultaneous inversion's corrections.

1 Introduction

In Earth's mantle, lateral variations in a given material property generally amount to only a few percent of the property's value over thousands of kilometers while radial variations reach one hundred percent over similar distances. Accordingly, much effort and progress was made toward the elucidation of spherically-symmetric Earth structure in early seismological and geophysical studies and studies of these radially-varying properties remain important today. However, systematic lateral variations do exist in the mantle and crust, at least, and with the advent of plate tectonics as a framework to help describe large-scale lateral variations, seismologists began studies of three-dimensional Earth structure on a global scale. The collection of data world-wide from sets of standardized instruments and the development of fast computers facilitated these studies.

This paper documents attempts to image the three-dimensional seismic P velocity heterogeneity in Earth's mantle. The approaches considered here involve the tomographic inversion of body wave travel time residuals and differ primarily in their treatment of the source location part of the dual problem. The seismic inverse problem to determine structural parameters of the medium (Earth) and parameters that describe the source is a complicated enterprise. The two sets of parameters are inextricably linked and the solution found for each set generally will not be unique. Attempts to retrieve one or both sets of parameters

typically concentrate on minimizing the influence of one set on the determination of the other set. This is the general approach we pursue here. We are most interested in the accurate estimation of Earth structure. First we try to simulate the general procedure by which tomographic inversions find models of Earth with body wave travel time data. We then find the effects of inaccurate source locations on the velocity model estimate and show how the velocity model estimate may be a reformulation of the source location problem.

The performance of the inversion algorithms is explored through simulations of the general procedure used to produce tomographic images of Earth's mantle from global earthquake data. A data set is constructed in a way that mimics the practice of the International Seismological Centre (ISC) as it collects observations world-wide, associates observations with seismic events, locates the events, and distributes the codified data to interested researchers. These data consist of arrival times at reporting stations and estimates of earthquake locations calculated in a one-dimensional Earth model. Because of the three-dimensional nature of Earth, the ISC locations are only approximations to the true earthquake locations, so we investigate the effects of mislocations on the velocities obtained in an inversion, and the ability of our simultaneous and progressive inversion techniques to correct mislocated earthquakes and find an accurate velocity model. To simplify the problem and highlight the effects of source mislocation in our controlled simulations we keep the numbers of data and model parameters small.

Finally, we invert real data supplied by the ISC. We use P arrival data from January 1964 through January 1987 and our inversion algorithms to solve for three-dimensional P velocity models of the mantle and source mislocations. We summarize results from both the simulations and real inversions in terms of what they tell us about the problem of ambiguous source locations and implications for contamination of our velocity models.

2 Mathematical development

The i^{th} arrival time from event j, that is recorded at a station k, may be represented as

$$(t_i)_j = \tau_j + T_i(\mathbf{r}_j, \mathbf{r}_k', c(\mathbf{r})) + (\varepsilon_i)_j, \tag{1}$$

where

τ_j = the origin time for event j,

$T_i(\mathbf{r}_j, \mathbf{r}_k', c(\mathbf{r}))$ = the travel time through the medium, $c(\mathbf{r})$, from event location, $\mathbf{r}_j$, to station location, $\mathbf{r}_k'$,

$(\varepsilon_i)_j$ = the reading error associated with ray i from event j,

and

$$i = 1,2,...,m_j, \qquad j = 1,2,...,n_e, \qquad k = 1,2,...,n_s;$$

where

m_j = number of arrival times reported for the j^{th} event,

n_e = number of events in the data set,

n_s = number of stations reporting arrivals in the data set.

In the general case, we have collected the observations $(t_i)_j$ but do not know any of the terms on the right hand side of equation (1). If we assume we know the velocity structure of the medium to within a few percent of the actual velocity, $c(\mathbf{r})$, we may take a first-order Taylor expansion about our model, call it $\hat{c}(\mathbf{r})$, and try to estimate the error in our model by reconciling the perturbation terms of the expansion with the deviations of observed arrival times from arrival times calculated through the reference velocity model. *Wielandt* [1987] carries out a set of synthetic experiments to investigate the validity of the linearity assumption inherent in this ray-theoretic formulation. Performing the Taylor expansion and discarding higher terms we get

$$(t_i)_j = \hat{t}_j + \delta\tau_j + \hat{T}_i(\mathbf{r}_j,\mathbf{r}_k',c(\mathbf{r})) + \delta T_i(\mathbf{r}_j,\mathbf{r}_k',c(\mathbf{r})) + (\varepsilon_i)_j, \tag{2}$$

where $\hat{t}_j$ is an estimate of event origin time calculated using the starting velocity model.

2.1 Contributions to the travel time discrepancy

Let

$$\hat{T}_i(\mathbf{r}_j,\mathbf{r}_k',c(\mathbf{r})) = T_i(\mathbf{r}_j,\mathbf{r}_k',c(\mathbf{r}))|_{\hat{\mathbf{r}}_j,\hat{\mathbf{r}}_k',\hat{c}(\mathbf{r})} \tag{3}$$

be the travel time for ray i connecting $\hat{\mathbf{r}}_j$ and $\hat{\mathbf{r}}_k'$ through velocity model $\hat{c}(\mathbf{r})$. The first-order term of the Taylor expansion may then be expressed as the sum of three terms:

$$\delta T_i(\mathbf{r}_j,\mathbf{r}_k',c(\mathbf{r})) = \delta T_i(\mathbf{r}_j,\mathbf{r}_k',c(\mathbf{r}))|_{\hat{\mathbf{r}}_k',\hat{c}(\mathbf{r})} + \delta T_i(\mathbf{r}_j,\mathbf{r}_k',c(\mathbf{r}))|_{\hat{\mathbf{r}}_j,\hat{\mathbf{r}}_k'} + \delta T_i(\mathbf{r}_j,\mathbf{r}_k',c(\mathbf{r}))|_{\hat{\mathbf{r}}_j,\hat{c}(\mathbf{r})}.$$

(4)

The first term on the right hand side of equation (4) represents the perturbation in the travel time due to a perturbation in the location of the earthquake's hypocenter. The second term represents the travel time perturbation due to perturbations in the velocity model. The third term represents contributions to the travel time anomaly that are unique to a particular station. Strictly, this third term represents travel time discrepancies due to poorly known station locations, but in practice the term serves to isolate the effects of velocity anomalies occurring in the vicinity of a station on a scale too small to be resolved by our model parametrization. Errors in observed travel time residuals resulting either from incorrect observations, such as instrument errors and systematic phase mispicks or misidentifications at a particular station, are also described by this "station" term.

We define the travel time residual to be the observed arrival time minus a predicted arrival time,

$$\delta(t_i)_j = (t_i)_j - (\hat{t}_j + T_i(\mathbf{r}_j,\mathbf{r}_k',c(\mathbf{r}))|_{\hat{r}_j,\hat{r}_k',\hat{c}(\mathbf{r})}). \tag{5}$$

Substituting equation (5) into equation (2) gives

$$\begin{aligned}\delta(t_i)_j &= \delta\tau_j + \delta T_i(\mathbf{r}_j,\mathbf{r}_k',c(\mathbf{r})) + (\varepsilon_i)_j,\\ &= \delta\tau_j + \delta T_i(\mathbf{r}_j,\mathbf{r}_k',c(\mathbf{r}))|_{\hat{r}_k',\hat{c}(\mathbf{r})}\\ &\quad + \delta T_i(\mathbf{r}_j,\mathbf{r}_k',c(\mathbf{r}))|_{\hat{r}_j,\hat{r}_k'} + \delta T_i(\mathbf{r}_j,\mathbf{r}_k',c(\mathbf{r}))|_{\hat{r}_j,\hat{c}(\mathbf{r})} + (\varepsilon_i)_j,\end{aligned} \tag{6}$$

The perturbation to the origin time, $\delta\tau_j$, may be viewed as a fourth hypocenter term. Then

$$\begin{aligned}\delta t_j^{hypocenter} &= \delta\tau_j + \delta T_i(\mathbf{r}_j,\mathbf{r}_k',c(\mathbf{r}))|_{\hat{r}_k',\hat{c}(\mathbf{r})}\\ &= \frac{\partial T_i}{\partial h_1}|_{\hat{r}_k',\hat{c}(\mathbf{r})}\delta h_{1_j} + \frac{\partial T_i}{\partial h_2}|_{\hat{r}_k',\hat{c}(\mathbf{r})}\delta h_{2_j} + \frac{\partial T_i}{\partial h_3}|_{\hat{r}_k',\hat{c}(\mathbf{r})}\delta h_{3_j} + \frac{\partial t_i}{\partial h_4}|_{\hat{r}_k',\hat{c}(\mathbf{r})}\delta h_{4_j},\end{aligned} \tag{7}$$

where

$$h_1 = \tau,\ h_2 = \theta,\ h_3 = \phi,\ h_4 = z.$$

In matrix notation,

$$\delta\mathbf{t}_j = \mathbf{H}_j\delta\mathbf{h}_j, \tag{8}$$

where

$\delta \mathbf{t}_j$ = vector of travel time residuals for event j,

$(H_{il})_j = \frac{\partial T_i}{\partial h_l}|_{\hat{\mathbf{r}}_k', \hat{c}(\mathbf{r})}$ = matrix of source mislocation partial derivatives (l=1,2,3,4),

$\delta \mathbf{h}_j = (\delta\tau, \delta\theta, \delta\phi, \delta z)_j$ = vector of hypocenter perturbations for event j.

The second term on the right hand side of equation (6) represents the deviation of our starting velocity model, $\hat{c}(\mathbf{r})$, from the actual velocity structure, $c(\mathbf{r})$,

$$\delta t_i^{model} = \delta T_i(\mathbf{r}_j, \mathbf{r}_k', c(\mathbf{r}))|_{\hat{\mathbf{r}}_j, \hat{\mathbf{r}}_k'}. \tag{9}$$

The travel time along a ray, S_i, is given by

$$t_i = \int_{S_i} \frac{ds}{c(\mathbf{r})}, \tag{10}$$

where $c(\mathbf{r})$ is the velocity of the medium. Our task is to determine $c(\mathbf{r})$ from a set of travel time observations t_i, i = 1,2,...M. This task is made more difficult by the implicit dependence of the ray path, S_i, on the velocity model, $c(\mathbf{r})$. Once again, we assume that our starting velocity model is within a few percent of the true structure and seek to reconcile the discrepancy by solving for the perturbation term. Let

$$\delta t_i^{model} = \delta T_i(\mathbf{r}_j, \mathbf{r}_k', c(\mathbf{r}))|_{true} - \delta T_i(\mathbf{r}_j, \mathbf{r}_k', c(\mathbf{r}))|_{\hat{\mathbf{r}}_k', \hat{c}(\mathbf{r})}, \tag{11}$$

$$= \int_{S_i} \frac{ds}{c(\mathbf{r})} - \int_{\hat{S}_i} \frac{ds}{\hat{c}(\mathbf{r})}.$$

Fermat's principle justifies the assumption that the raypath persists relatively unchanged in the presence of small three-dimensional velocities anomalies. This allows us to perform both line integrals along the initial raypath, i.e.,

$$\delta t_i^{model} = \approx \int_{\hat{S}_i} \left(\frac{1}{c(\mathbf{r})} - \frac{1}{\hat{c}(\mathbf{r})}\right) ds,$$

$$\approx -\int_{\hat{S}_i} \frac{\delta c(\mathbf{r})}{\hat{c}^2(\mathbf{r})} ds, \tag{12}$$

where $\hat{S}_i$ is the path of the i^{th} ray through the starting velocity model, $\hat{c}(\mathbf{r})$.

In order to represent the function of velocity perturbations over the medium of interest, we must choose a set of basis functions. Our approach follows *Nolet* [1987] and divides the medium under investigation into non-overlapping volume elements, or voxels. Let

$$f_k(\mathbf{r}) = \begin{cases} v_k^{-1/2} & \text{if } \mathbf{r} \text{ is in cell } k \\ 0 & \text{elsewhere} \end{cases}, \tag{13}$$

where v_k is the volume of cell k. The functions f_k form a basis that spans a subspace of the Hilbert space of all possible velocity models, $c(\mathbf{r})$. Since the cells do not overlap,

$$\int_{volume} f_k(\mathbf{r}) f_l(\mathbf{r}) d^3\mathbf{r} = \delta_{kl}. \tag{14}$$

Choosing a model parametrization introduces bias into the inversion. Depending on the geometry of the inverse problem and nature of the medium under investigation, a particular model parametrization may or may not allow the accurate reconstruction of interesting features of the medium. It may, in fact, require an inaccurate (i.e., smeared or aliased) estimation of the model simply because of limitations in its representation of features. *Michelena and Harris* [1991] suggest a way to make the model parametrization more flexible and complete in its representation of model anomalies sampled by a data set. Their representation acknowledges the finite width of the zone sampled by a given seismic ray and seeks to construct a solution in terms of the portions of Earth sampled by these "fat" rays. They call this representation a parametrization based on "natural pixels." Further approaches to map the sensitivity of the recorded arrival to portions of the medium have been developed by *Luo and Schuster* [1991], *Woodward* [1992], *Stark et al.* [1992], and *Vasco and Majer* [1992]. None of these approaches is currently feasible for mantle-scale studies. A voxel basis is also local and offers orthogonality as well as a conceptually simple representation of Earth. Each model parameter represents a physical location in the model. The model resolution and covariance thus carry explicit geographical information. A voxel basis also results in a sparse coefficient matrix; this sparseness can be exploited to perform the computations efficiently. A global basis, such as spherical harmonics, does not offer the simplicity, sparseness, or geographical correspondence of voxels.

Choosing the set of functions described in equation (13), we may represent the function of velocity perturbations as a linear combination of basis functions,

$$\delta c(\mathbf{r}) = \sum_{k=1}^{n} \gamma_k f_k(r). \tag{15}$$

Substituting equation (15) into equation (12) results in an expression for the travel time perturbations in terms of velocity perturbation basis functions,

$$\delta t_i^{model} = \sum_{k=1}^{n} -\int_{S_i} \frac{\gamma_k f_k(\mathbf{r})}{\hat{c}(\mathbf{r})^2} ds = \sum_{k=1}^{n} A_{ik}\gamma_k, \tag{16}$$

where

$$A_{ik} = -\int_{S_i} \frac{f_k(\mathbf{r})}{\hat{c}(\mathbf{r})^2} ds.$$

In matrix form,

$$\delta \mathbf{t}^{model} = \mathbf{A}\boldsymbol{\gamma}. \tag{17}$$

We express the "station" term of equation (4) as

$$\delta \mathbf{t}^{station} = \mathbf{S}\boldsymbol{\mu}, \tag{18}$$

where

$$S_{ik} = \begin{cases} 1 & \text{if } k = \text{station number} \\ 0 & \text{if } k \neq \text{station number'} \end{cases}$$

μ_k = the station correction for the k^{th} station.

Substituting equations (8), (17), and (18) into equation (6) for all rays ($i = 1,2,...,m_j$) of all events ($j = 1,2,...,n_e$) we find the problem we wish to solve is now

$$(\delta t_i)_j = (\delta t_i^{hypocenter})_j + (\delta t_i^{model})_j + (\delta t_i^{station})_j, \tag{19}$$

or

$$\delta \mathbf{t} = \mathbf{H}\,\delta \mathbf{h} + \mathbf{A}\,\boldsymbol{\gamma} + \mathbf{S}\,\delta\boldsymbol{\mu}, \tag{20}$$

where

$\delta \mathbf{t} \in R^{M\times 1}$ = vector of travel time residuals,

$\mathbf{H} \in R^{M\times 4n_e}$ = matrix of partial derivatives for all events,

$\delta \mathbf{h} \in R^{4n_e\times 1}$ = vector of perturbations to the hypocenters,

$\mathbf{A} \in R^{M \times n_p}$ = matrix of velocity perturbation coefficients,

$\boldsymbol{\gamma} \in R^{n_p \times 1}$ = vector of coefficients in the expansion of perturbations to the starting model,

$\mathbf{S} \in R^{M \times n_s}$ = matrix of partial derivatives for stations,

$\boldsymbol{\delta\mu} \in R^{n_s \times 1}$ = vector of station corrections,

M = number of data (reported arrivals),

n_e = number of events,

n_p = number of model blocks,

n_s = number of reporting stations.

2.2 Simultaneous inversion

The simplest and most direct way solve equation (20) is to combine the three coefficient matrices and solve for all parameters simultaneously, i.e.

$$\left[\mathbf{H} \mid \mathbf{A} \mid \mathbf{S}\right] \begin{bmatrix} \boldsymbol{\delta h} \\ \hline \boldsymbol{\gamma} \\ \hline \boldsymbol{\delta\mu} \end{bmatrix} = \boldsymbol{\delta t}, \tag{21}$$

or

$$\mathbf{Gx} = \mathbf{b}, \tag{22}$$

where

$$\mathbf{G} = \left[\mathbf{H} \mid \mathbf{A} \mid \mathbf{S}\right],$$

$$\mathbf{x} = \begin{bmatrix} \boldsymbol{\delta h} \\ \hline \boldsymbol{\gamma} \\ \hline \boldsymbol{\delta\mu} \end{bmatrix},$$

and

$$\mathbf{b} = \boldsymbol{\delta t}.$$

H and **S** are first scaled so that each row has the same euclidean norm as the same row of **A**. In this study

we did not solve for the station term. In what follows the effects of the station term could be dealt with in a fashion similar to the treatment of the source term, but the large numbers of data and parameters involved in our whole-mantle inversions render the full problem unwieldy. We expect the deleterious effects of the station errors on our retrieval of velocity parameters to be small compared to the effects of source mislocation.

2.3 Progressive inversion

There are two reasons why we may choose not to combine matrices and solve for all parameters simultaneously. First, since re-locating the hypocenter of each event consists of estimating four terms: origin time plus three spatial coordinates, the number of hypocentral parameters totals $4n_e$, where n_e is the number of events in the data set. Neglecting station terms, the combined matrix would therefore have dimensions $M \times (n_p+4n_e)$, resulting in considerable demands for core memory and mixing different classes of parameters. More importantly, it turns out that we may exploit the natural separation of the parameters to solve for each set of parameters in a step-wise fashion. This approach follows *Pavlis and Booker* [1980], *Spencer and Gubbins* [1980], *Jordan and Sverdrup* [1981], and *O'Connell and Johnson* [1991], among others. It allows a more detailed analysis of resolution and uncertainty in the determination of mislocation terms than would be possible otherwise and ultimately produces estimates of velocity parameters that are not affected by small changes in source locations. The idea is to find an orthogonal transformation from each hypocenter's matrix of partial derivatives, call it $\mathbf{H}_j$ with n_j reported observations, so that only the first four elements of the event's travel time residual vector have non-zero projections into the hypocentral parameter space. Then n_j-4 components have non-zero projections into the space of velocity parameters and these are independent of the hypocenter. Actually, the number of independent data providing information to the specification of parameters is equal to the rank of the original, unrotated matrix $\mathbf{h}_j$, where $0 \le rank(\mathbf{h}_j) \le 4$. *Pavlis and Booker* [1980] call this operation an "annulling transformation" because its effect is to separate the problem involving, for example, two different classes of parameters into two problems, the second of which is independent of the first class of parameters. The independent problem involves data that have been "annulled" with respect to the first parameter class. A complete development of the tomographic, progressive inversion method may be found in the Appendix. Ultimately we are left with a linear system equations of the form (equation A6)

$$\mathbf{Gx} = \mathbf{b} \tag{23}$$

that we must solve to find the structural parameters, **x**. $\mathbf{G} \equiv \mathbf{A}_N$ is the portion of the rotated matrix **A** that contributes only to the rotated travel time residuals, $\mathbf{b} \equiv \delta\mathbf{t}_N$. The sampling of Earth provided by our data set will cause some of the voxel parameters to be overdetermined while others are underdetermined. Some damping and smoothing must be introduced to regularize the problem and ensure a physically-plausible solution. The details of these procedures and the choices we made are presented in *Pulliam et al.* [1992] and will only be summarized briefly here. Damping is performed by effectively adding a small constant to the diagonal of the $\mathbf{G}^T\mathbf{G}$ matrix, although this square matrix is never formed explicitly. In both the simultaneous and progressive inversions, the solution for model parameters is found via the conjugate-gradient LSQR algorithm in a row-active implementation. For details of the LSQR algorithm, see *Paige and Saunders* [1982] and *Nolet* [1985]. Applications of the LSQR algorithm to whole-mantle inversions are performed by *Inoue et al.* [1990] and *Pulliam et al.* [1992]. Another whole-mantle study in which the formal least squares solution was found from an LU decomposition of the mantle tomographic coefficient matrix [*Vasco et al.*, 1991] indicates that the LSQR solution is an excellent approximation to the least squares solution. In order to simplify the analysis and comparison that are the purposes of this study, we choose not to apply a roughness penalty during the inversion. Our intent is to identify the effects of source mislocation on the velocity parameter estimates and an added operator would only serve to obscure those effects.

3 Synthetic tests of the algorithms

In order to test the effectiveness of our algorithm in retrieving both velocity structure and source mislocations we conduct a controlled simulation of the general procedure used to produce tomographic images of the mantle from synthetic global earthquake data, similar to the data supplied by the ISC. These data consist of arrival times at reporting stations and estimates of earthquake locations calculated in a one-dimensional Earth model. The steps we follow to perform these simulations are outlined in figure 1. To produce synthetic data such as those provided by the ISC we distribute sources and receivers around a model Earth (step 1). Receivers locations are chosen from among the locations of actual stations that report to the ISC. We want to address the problem of source mislocation in a three-dimensional medium, and not the problem of poor ray coverage of Earth, so we intend to distribute sources and receivers adequately to allow accurate retrieval of velocity anomalies given "true" source locations (i.e., the starting source

locations). To this end, we place nine sources around Earth, located at depths ranging from 40 to 180 km, and a total of 207 stations, for an average of 45 reporting stations per event (see figure 2). To check the adequacy of the geometrical constraint placed on the source location by the ray coverage we immediately re-locate the introduced sources using a damped least-squares procedure and the one-dimensional Jeffreys-Bullen (JB) P velocity model (step 1a). At this point, no velocity anomalies are present in the model. The standard errors on these direct re-locations tell us the best we can expect to do later, when we correct the deliberately mislocated sources.

Next we introduce four velocity anomalies (step 2) and calculate travel times through the new 3-D model (step 3). The raytracing performed here is for a fully 3-D medium. Travel times are calculated through the 3-D model by a shooting method involving the direct numerical integration of the eikonal equations that uses a Newton-type search for the solution to the two-point boundary value problem. We parametrize the model Earth with approximately equal-area voxels, 30° x 30°, at the equator and six layers, which makes each layer about 500 km thick and gives a total of 276 voxels. Highlighted in white and black in figures 3ab are the voxels in which negative and positive velocity anomalies are introduced. All four anomalous voxels are located in these two layers. Magnitudes of the anomalies range from 1.5% to 2.0% of the local velocity. These anomalies are located in reasonably well-sampled voxels, but not the most heavily sampled. Ray sampling is shown in figure 4.

Our choice of a block model parametrization causes problems for the 3-D raytracing required to produce synthetic data. The eikonal equations can only be solved practically for a reasonably smooth model. Instead of a smooth model, our blocks confront the raytracer with an overwhelming set of discontinuities in both lateral and radial directions that cause unwarranted and physically implausible complexity. We smooth an introduced, "spike" anomaly by placing the anomalous velocity at the center point of its assigned voxel and requiring the value to decrease linearly toward the voxel boundaries. Thus the velocity experienced by each ray that visits an anomalous voxel will be well below the peak value located at the voxel center. This is a minor point that affects only the velocity perturbations returned by our inversion scheme and not the relative values as they are altered by the effects of source mislocation. To find the absolute values, we perform an inversion based on the travel times through the 3-D model from the true source locations (step 3a). In practice, these true locations are rarely known. The purpose of this exercise is to construct a controlled simulation in which we isolate the effects of just one type of error. Here we retain control of the velocity

problem and seek to isolate the effects of source mislocation.

At this point, we have synthesized data analogous to those provided to the ISC by observers located around the world. Next we use the travel times through the 3-D model as arrival times to re-locate the sources in a 1-D model (step 4). Again we use the JB model. Now we have a set of data analogous to the catalog provided by the ISC to researchers world-wide. Next we calculate residuals by subtracting the synthetic arrival times from the travel times through the JB model from the new, re-located source (step 5) and invert these residuals in three ways:

1.) directly, neglecting source mislocation terms (step 6a),

2.) simultaneously for velocity and source terms (step 6b), and

3.) by means of the progressive inversion scheme, in which the velocity problem is separated from the source mislocation problem and solved separately (step 6c).

In each of these cases we use the conjugate-gradient projection method LSQR. Gaussian noise is added to the synthetic data before inversions are performed. The mean and variance of the added noise are determined from the remaining variance of ISC travel time residuals in inversions of real data. The random deviates are adjusted to the appropriate scale for this test problem. Finally, we compare the corrected source locations to the true locations and the estimates of the four velocity anomalies produced in each inversion, along with smearing and artifact anomalies (step 7).

3.1 Source mislocations

Tables 1-9 show the source corrections resulting from both the simultaneous and progressive inversions. The tables show, for each source parameter, the "a priori" standard error in the first column. This is the standard error from the first computed location of the sources introduced to the JB model and "located" with the damped least squares program in the JB model (with no anomalies present). These standard errors represent the best our algorithm can hope to achieve with the given ray coverage. The second column contains the initial parameter offset. For each parameter, these are the amounts the source re-located in the 3-D model differs from the true source location. Depending on the proximity of the introduced anomalies to the earthquake hypocenter, a given hypocenter will be moved a great deal (e.g., events 4 and 5) or only slightly (e.g., events 1, 2, and 7). Column 3 contains the results after source corrections obtained from simultaneous inversion have been applied to the initial parameter offset and it shows how far away the corrected location is from the true source location. The fourth column shows how much the simultaneous inversion improved

the source location. Columns 5 and 6 present the same information as columns 3 and 4, but for corrections that emerge from the progressive inversion. To interpret these results, compare the second column to the first column of each table to see if the improvements indicated are significant. Is the initial offset greater than the "a priori" standard error? If so, does the correction applied reduce the parameter offset or increase it?

For example, the origin time, latitude, and longitude parameters for Events 1 and 7 are not significantly offset. Therefore the resulting corrections may be misleading. Events 2, 3, and 9 have unusually small initial offsets, locations this accurate would not require corrections anyway. For both the simultaneous and progressive inversions, event 4 shows significant improvement of an initially poorly located source. Perhaps the latitude and longitude terms are less significant. Event 5 has the most dramatic results. All parameters are initially offset a significant amount and for the progressive inversion, all but the longitude term were corrected to well within the "a priori" standard error. Particularly with respect to the origin time and source depth parameters, the progressive inversion performed better than the simultaneous inversion for these two most significant events, 4 and 5, as it generally did throughout these tests. Of particular concern is the poor estimation by the simultaneous inversion of the corrections to origin time and depth. Events 6 and 8 show good, though mixed, results. In all cases in which a parameter is offset an amount greater than the standard error, the correction produced by the progressive inversion reduces the offset to within the standard error. The simultaneous inversion produced just one exception to this rule (the longitude correction for event 8). In cases in which the initial offset is still within the standard error the correction usually reduces the offset further, but it may also result in a greater offset from the true source. In all but one of the cases in which the offset rendered by the progressive inversion is an increase over the initial offset, the final offset is still within the parameter's "a priori" standard error. This is true for all but four of the offsets rendered by the simultaneous scheme. Apparently once an offset is within the standard error, attempts to decrease the mislocation further result in a waffling about within a range of the true value roughly bounded by the standard error. This "loose" bound, rather than than a "hard", inviolable bound is expected for the standard error. We tested this further by performing another iteration of the imaging scheme in which our source location estimates are updated by applying the corrections resulting from the first iteration and the entire algorithm is repeated, based on the new locations. Indeed, in every case in which the first iteration's offset still lay outside the "a priori" standard error, the second iteration improved the offset to within this standard error. In

addition, for the progressive inversion five more parameters corrected after the first iteration to within the standard error jumped outside of the standard error after the second iteration. Perhaps if the initial offsets were larger, and generally more significant according to the "a priori" standard errors, the second iteration would be warranted and helpful. In our test case, the second iteration produced negligible improvement and, in fact, resulted in a degradation of source location estimates as often as improvement. The important result, however, is that the "a priori" standard error estimates allow the reliable determination of the significance of a particular correction. These standard errors are supplied by the ISC along with their location estimates.

Ideally, sources would be re-located in a three-dimensional model rather than with corrections produced as a by-product of an inversion for velocity. Both the location and velocity estimation problems are nonlinear and should be approached with an optimization scheme. But an iterative scheme for a fully three-dimensional Earth that incorporates enough data and parameters to constrain interesting features of Earth is beyond our computational capacity at present. At this stage our greatest interest is in finding an inversion scheme that decouples the source location and velocity problems as much as is possible. In the next section we explore the consequences of removing the contributions of source mislocations from the travel time residual for our retrieval of a 3-D velocity model.

3.2 Velocity model

Table 10 shows estimates for the four input anomalies and a fifth entry for the next largest value emerging from the inversion. This fifth entry is the largest artifact anomaly and does not represent the same voxel across the bottom row of the table. Column 2 shows the number of rays sampling each model block. The most-sampled voxel had 96 hits; several voxels had more than 72 hits. The 3-D anomalies we introduced to the JB model are indicated as "peak" anomalies in column 3. To find the actual image we are trying to recover, neglecting the effects of imperfect ray coverage (i.e. to assess the effects of smoothing the four input "spikes"), we invert residuals calculated by subtracting the synthetic travel times from travel times through the JB model from the *true* source locations. This result, listed in column 4 of Table 10, contains the effects of imperfect ray coverage, which introduces a skewed average velocity depending on what parts of each voxel are sampled by rays and the type of function employed to smooth the input velocity "spikes". Columns 5 and 6 show the results of directly inverting the data from mislocated sources. Neglecting the effects of source offset results in underestimating the velocity anomalies by over 50% in some cases, and

produces artifact anomalies with absolute values greater than estimates for true values. Columns 7 and 8 show the same information for the simultaneous estimation of source and velocity terms. Note the overshoot in two cases, gross underestimate in one case, and the large artifact anomaly. The last columns of Table 10 show the results of our progressive inversion scheme. Here we retrieve a much greater portion of the velocity, with slight overshoot in one case, and with artifacts attaining a maximum magnitude of about one quarter the smallest true anomaly.

4 Inversions of real data

4.1 Data selection

The data inverted in this study were obtained from the catalog of the International Seismological Centre (ISC) for the period January 1964 through January 1987. To avoid contamination of our mantle phases by Earth's core we limit the range of our coverage to epicentral distances between 0° and 96°. The scatter caused by refractions from the 400 km and 670 km discontinuities, at about 15° to 25°, is dealt with in the inversion process by weighting each summary ray by the inverse of the standard error of travel time residuals as a function of delta. To ensure that sources are well-located, each event must have a minimum of forty reporting stations, and source depths, as reported by the ISC, must be greater than 0 km and less than 70 km. In addition, maximum standard errors for the ISC locations must be 1 sec for origin time, 0.1° for both latitude and longitude, and 10 km for depth. We discard all events located by the ISC at Earth's surface, but retain events located at the other default depths. To ensure adequate and reasonably uniform ray coverage of Earth we keep a maximum of twenty-five events in each voxel. The set of events retained for each voxel always includes the events with the most observations. In this study we do not form summary rays. All observations are corrected for ellipticity by numerical integration along the raypath of the travel time perturbation arising from deviations of a hydrostatic figure from a sphere. Lengths of ray segments in voxels are found by integrating distance along the curved raypath and finding the intersections of rays with voxel boundaries. Rays associated with residuals greater than seven seconds are discarded. Approximately 345,000 rays satisfy these criteria. Figures 5ab show the locations of the selected events and seismographic stations, respectively. Figure 6 shows a histogram of travel time residuals binned in 1° intervals associated with sources located by the ISC at depths greater than 0 and less than or equal to 70 km.

4.2 Model

The starting model used in this study is a one-dimensional, spherically-symmetric P velocity model modified from *Jeffreys* [1960]. The model mantle is divided into 14 layers, approximately 200 km thick, with radial boundaries located at Earth's major discontinuities. Each layer contains 406 approximately equal area voxels, 10° x 10° at the equator, for a total of 5684 model parameters. The exceptions to the 200 km thick layers occur in the upper mantle, in order to place a radial boundary at the 670 km discontinuity (resulting in a 270 km thick layer) and above the core-mantle boundary, where the lowermost layer is 228 km thick. One layer of our model parametrization is shown in figure 7.

Figures 8a-h show the ray coverage of the mantle provided by the approximately 345,000 observations included in our data set. Sampling is described in terms of the number of rays that traverse each voxel. The most-sampled voxel has over 50,000 samples. Only 166 of 5684 voxels are unsampled. Figure 8a shows the clear demarcation of plate boundary source regions that, along with Asia, North America, Europe, and Australia, are well-sampled. In contrast, other regions tend to be quite poorly-sampled. There are also large oceanic areas in the first few layers that are completely unsampled by our data set. These voxels do not enter into the inversion. The next depth layer, figure 8b, shows a broadening of the well-sampled regions and a slight reduction of the unsampled oceanic areas. At 400-670 km and 670-870, figures 8cd, these trends continue, and by the mid-mantle, figures 8ef, virtually all voxels are sampled. In general, sampling becomes more homogeneous with depth and at the bottom of the mantle, figures 8gh, the sampling is much more uniform than in the first layer. Note in all eight figures the strong bias toward the northern hemisphere, in general, and toward continents in particular. However, in absolute numbers the sums of ray segments in voxels decrease with depth, even as more voxels are sampled in each layer. Table 11 details the average number of hits for sampled voxels in each layer along with the the average sum of ray segments in a voxel at a given depth and the number of voxels sampled in each depth interval. These averages include only voxels that have non-zero sampling. The trends in Table 11 show that while homogeneity of sampling increases with depth, voxels tend to be less frequently traversed by recorded seismic rays.

4.3 Inversion results

Inversions of the ISC data were performed directly, neglecting source terms, simultaneously for source mislocation and velocity terms, and progressively for each set of terms. The resulting models are named *isc10_direct*, *isc10_sim*, and *isc10_pro*, respectively. The weights applied in each inversion are identical and the LSQR algorithm is performed for 20 iterations in each case. Convergence was determined by the

relative change of the residual norm after each iteration. At 20 iterations, each model produces a slightly different variance reduction of the travel time residual distribution. For model *isc10_direct* the variance reduction is 12%, for model *isc10_sim* it is 14%, and for model *isc10_pro* it is 16%. Minimum and maximum velocity perturbations are [–1.4%, 1.9%] for *isc10_direct*, [–1.8%, 1.8%] for *isc10_sim*, and [–2.2%, 2.3%] for *isc10_pro*.

Figures 9-11 show six of the fourteen layers for each inversion. Despite the large voxel size, the top layers, 0-200 km depth (figures a) and 200-400 km (figures b), show quite strong correlations with surface tectonics. All models show fast anomalies in the Asian, Australian, and North American shield regions. The Indian subcontinent and southern Africa are consistently fast in all the models' top layers. Also in the top layers, a ring of slow anomalies surrounds the Pacific basin, though the ring is not as continuous a feature in the progressive model. Nevertheless, the Central American subduction zone, Nazca Plate, Galapagos hotspot, northwestern South America and all of the North American Great Basin and Range Province, including the Yellowstone and Raton, New Mexico hotspots, are covered by a broad, unusually slow anomaly. All models share this feature in the 0-200 km layer. In the 200-400 km depth range *isc10_direct* and *isc10_sim* show an intruding fast anomaly that extends across northern Mexico and Baja California while *isc10_pro* remains slow, consistent with the layer above. The first two models show this same fast anomaly in the 400-670 km depth range while *isc10_pro* remains slow.

Elsewhere around the Pacific, slow backarc basins appear to compete with fast subducting lithosphere to claim the dominant anomaly for a particular region. From southern Alaska westward along the Aleutian island arc all the models begin with a fast anomaly and switch to a slow anomaly as the backarc basin comprises a larger portion of the next voxel to the west. Still further west, the next voxel also includes parts of the Kurile arc as well as the Aleutian arc and model *isc10_pro* returns a positive anomaly while *isc10_direct* and *isc10_sim* are marked by slow anomalies. Similar differences between the first two models and the progressive model appear in the northern Japanese, Mariana, Philippine, Micronesian, Tongan, and Chilean subduction zones.

Further similarities between all three models include slow anomalies in East Africa, which are associated with a broad slow anomaly that persists through the first three layers of each model, the Mediterranean Sea, and the Hawaiian/Emperor hotspot. Another common feature is the abrupt change at the 400-670 km layer in each model of the sign of the anomaly associated with continental shields. Only the Australian shield

remains largely a fast region. In the northern hemisphere, slow anomalies have displaced the fast anomalies in the continents' southern portions.

Further differences between the models arise in a comparison of mid-ocean ridges. Models *isc10_direct* and *isc10_sim* are fairly consistently marked by slow anomalies in the top layers, with exceptions arising almost exclusively in the southern hemisphere, where ray coverage is relatively poor. *isc10_pro* shares the same negative sign for most anomalies, but ridges in the southern hemisphere are more consistently slow and the mid-Atlantic ridge is not marked by the same broad slow anomaly as in the first two models.

Figures 9d-f, 10d-f, and 11d-f present the three models for the 1270-1470 km, 1470-1670 km, and 2470-2670 km depth ranges, respectively. In the mid-mantle (figures de), models *isc10_direct* and *isc10_sim* show larger-scale anomalies, less broken by small-scale intrusions, than does model *isc10_pro*. Surprisingly, continental regions in the northern hemisphere are generally associated with fast anomalies and oceanic regions are generally associated with slow anomalies. Continents in the southern hemisphere are not marked by fast anomalies. Most striking are fast anomalies beneath eastern North America, the Caribbean, and northwestern South America, and the fast features beneath Tonga and Japan/eastern Asia. The fast anomaly beneath eastern North America and the Caribbean appears in the same location as a large S-velocity anomaly reported by *Grand* [1987]. Similar features for P velocity appear in the inversions performed by *van der Hilst and Engdahl* [1991] for the Caribbean and Central American region. The fast feature beneath Tonga broadens and continues to dip to the west to a depth of 1670 km. Beneath Japan and eastern Asia the fast anomaly is diffuse but extends all the way to the core-mantle boundary.

The 2470-2670 km depth layer (figures f) shows a more broken, fast pattern beneath the Pacific basin at the mantle's bottom. A ring of slow anomalies around the Pacific is emerging, but is not nearly as strong as the ring observed by *Dziewonski* [1984], *Morelli and Dziewonski* [1985, 1986], and *Clayton and Comer* [1983; *Hager and Clayton*, 1989] in the lowermost mantle. Seeking to avoid contamination of our data by diffractions at the core-mantle boundary, we impose an epicentral distance limit of 96° on our observations. The resulting ray coverage does not allow us to be confident of our results for the lowermost layer (D"). Regardless of differences between our models and models produced previously by others, it is clear that differences between the upper mantle layers of our three models are greater than are differences between layers of the lower mantle.

4.4 Comparison of small-scale model features

The upper mantles of our three models apparently differ from each other more than do the lower mantles. To test this observation more rigorously at the scale of individual model blocks we employ a statistical correlation technique. Because we do not know the probability distribution function from which our sample model values are drawn, we prefer a non-parametric procedure, and since we already know that our models generally differ in the amplitudes of individual model values, we are most interested in a technique that compares the heterogeneity patterns of two models rather than the individual values of heterogeneity. For these reasons we choose to evaluate model layer correlations with a non-parametric rank-order correlation procedure. When comparing a given layer of two models we replace each velocity value from the first model with its rank among the $N-1$ other values in the same layer, and do likewise with values from the same layer of the second model. Now the series to be examined for correlation consist of integers, 1 to N, that are drawn from a perfectly known distribution. If some of the velocity values are identical, they are assigned rank equal to the mean of the rank they would have had were they distinct. This assigned rank will not, and need not, necessarily be an integer. Regardless, the sum of all assigned ranks will equal the sum of the numbers 1 to N. What results is two sets of rankings, generally the integers 1 to N, for which statistics have been developed and are well-used. As the most straight-forward of the common rank-order correlation statistics we choose to employ the Spearman statistic, which is defined as

$$r_s = \frac{\sum_{i=1}^{N}(R_i-\bar{R})(S_i-\bar{S})}{\left[\sum_{i=1}^{N}(R_i-\bar{R})^2\right]^{1/2}\left[\sum_{i=1}^{N}(S_i-\bar{S})^2\right]^{1/2}} \tag{24}$$

where

R = series indicating the rankings of the first model's velocity values for a given layer,

S = series indicating the rankings of the second model's velocity values for the same layer.

Figure 12 shows the Spearman rank-order correlations between layers of each set of two models. Clearly the models *isc10_direct* and *isc10_sim* are quite similar even at the scale of individual model blocks. Still, the small differences that do exist tend to be located in the upper portions of the models. These differences

disappear with depth. Correlations between models *isc10_sim* and *isc10_pro* are fairly consistent throughout the lower mantle, though a small peak appears again at the 1270-1470 km depth layer. In the upper mantle, however, the top two layers display a marked decrease in correlation. This concentration of differences in the top layer, in which all our sources are located, and the next lower layer indicates that our inversion procedures' different treatment of the source location terms results in important differences only for these layers at short wavelengths.

4.5 Comparison of large-scale model features

To serve as a low-pass filtering procedure, we calculate surface spherical harmonic series expansions to degree and order 10 by integration around the globe for each coefficient. The associated Legendre polynomials are fully normalized. Figure 13 show the total power in the series expansions for each model plotted as a function of depth. The distribution of power with depth is quite similar for *isc10_direct* and *isc10_sim*, though the total power contained in the direct model is greater than that in *isc10_sim*. *isc10_pro* shows a slightly different pattern. Unlike the first two models, the most heterogeneous layer is the topmost, 0-200 km. The anomalously low power in the 200-400 km layers of all our models is probably due to the fact that rays bottoming in this layer, which emerge at the epicentral distance range $15° \leq \Delta \leq 20°$, have the largest variance of all the travel time residuals. These rays are the most sensitive to velocity perturbations in the 200-400 km layer, but in our inversion their influence on the final model is downweighted by the inverse of the residuals' standard errors. The transition zone, 400-670 km, contains the highest power in models *isc10_direct* and *isc10_sim*, indicating the greatest heterogeneity in these models occurs at these depths. Note that the absolute magnitudes of these transition zone power totals are comparable to, and do not exceed, the power in the *isc10_pro* transition zone. Because our starting model does not contain discontinuities, our theoretical ray coverage of the transition zone is more uniform than is the case for models of the mantle that include discontinuities at 400 and 670 km depth. As a result, we are probably mapping more power into the transition zone for all three models than is justified. Deeper in the mantle a relative peak appears at about 1300 km depth and is followed by diminished heterogeneity at greater depths. This increase in power at the 1270-1470 km depth layer may be attributed to anomalously large $l = 1, 2$, and 3 components in all three models. At the bottom of the mantle, *isc10_direct* and *isc10_sim* show a dramatic increase in heterogeneity while the *isc10_pro* shows only a modest increase. The drop in power from the 2470-2670 km layer to the lowermost layer, 2670-CMB, is probably due to the

poor ray coverage in this bottom layer that results from our epicentral distance limit of 96°.

Figures 14-16 show, for each model, the power in series expansions of each layer as a function of angular degree. As figure 13 would lead us to expect, power at all degrees in the top two layers of models *isc10_direct* and *isc10_sim* is smaller than the power contained in the top two layers of *isc10_pro*. Particularly striking are the large values of the $l = 5$ and $l = 6$ components and the consistent importance of the $l = 6$ component throughout the upper third of the mantle. The finding of a large $l = 2$ component in the transition zone confirms previous reports, but a prominent $l = 3$ also appears in all models. The progressive model shows a large $l = 6$ harmonic as well. In the mid-mantle, 1070-1670 km, the $l = 2$ and 3 components rise above the higher-degree harmonics with nearly the same pattern for all models. More differences arise in the lowermost mantle, where the dominant heterogeneity of model *isc10_pro* is concentrated in the $l = 3$ term, while the first two models show anomalous $l = 1$ components.

Since sign information is not included in power calculations, figures 14-16 do not offer any clues as to how the distribution patterns for all layers combine constructively or destructively to form a pattern for the whole mantle. Figures 17-19 show the power in the spherical harmonic expansions for the respective models averaged through the whole mantle and through the upper and lower mantle separately. The averaging is performed on the the individual harmonic coefficients, weighted at each layer by the square of the layer mid-point's radius, which normalizes the power in each layer to the layer's surface area. Here, differences between the models appear most dramatically. For the upper mantle the *isc10_pro* (figure 19) power spectrum shows a dominant $l = 6$ component, along with prominent $l = 2$, 5, and 8 terms. In contrast, the *isc10_direct* (figure 17) and *isc10_sim* (figure 18) power spectra show no constructive patterns other than a quite prominent $l = 2$ pattern. When averaged over the lower mantle alone the three models show quite similar patterns, apart from a slightly more prominent $l = 2$ harmonic in the progressive model. Apparently there is some type of compensation at work, either numerical tradeoff between layers of our computed models or physical compensation of velocity heterogeneity in the real Earth. When individual layer series are averaged over the entire mantle, the prominent patterns of the *isc10_pro* upper mantle nearly disappear and the components of the *isc10_direct* and *isc10_sim* upper mantles decrease in power. Only the large $l = 2$ term survives the whole mantle average.

4.6 Source Corrections

Figures 20 and 21 show source correction vectors produced by the simultaneous and progressive inversions, respectively, for the same 400 events. These relocations are representative of the corrections required by each inversion procedure for the 3077 events used in this study. In each case the starting location (found by the ISC) is indicated with either an asterisk or hexagon and a scaled vector points in the direction of the correction required by the latitude and longitude adjustments. For each event the direction of the depth correction is indicated by the type of symbol marking the relocation vector's endpoint. Events that receive a shallowing correction are marked with asterisks; events that are relocated deeper are marked by a hexagon. Origin time corrections are not shown. Both figures 20 and 21 are scaled to the same maximum vector length.

The most striking feature of these figures is that the corrections produced by the progressive inversion (figure 21) are clearly larger than the corrections produced by the simultaneous inversion (figure 20). Overall the progressive corrections are generally two to four times the simultaneous corrections, although in some cases the progressive corrections are far greater. The corrections required in remote regions, where we might expect the constraints provided by the station distribution to be relatively weak, are not generally the largest in either case. The simultaneous inversion, particularly, produces small corrections in such remote regions as the Carlsberg and Indian Ocean ridges. The progressive inversion produces much larger corrections, but these corrections are not generally larger than the corrections produced in well-instrumented regions such as western North America, the eastern Mediterranean, and the Japanese subduction zone. The progressive corrections do not claim to be unerringly correct, they simply find that more of the travel time residual can be explained by moving the source than does the simultaneous, which finds a best-fitting location. Recall that poorly-located events, as determined by the standard errors of the ISC locations, were culled from our data set originally. Each source used here is one of the best-constrained of the ISC events located in its vicinity.

Though the corrections from the two inversions differ in size, some recognizable patterns and similarities emerge from a comparison of figures 20 and 21. In the northern parts of Japan, both sets of corrections are overwhelmingly oriented northward and slightly west of north. These corrections are some of the largest in each set. Whether this direction is correct, or at least expected from what we know of the location of lithosphere subducting underneath Japan, depends on whether the events actually occur predominantly on one side of the descending slab or are well-distributed throughout the slab. The depth corrections are moderate

($5\ km < \delta h \leq 10\ km$) for both inversions. Along the west coast of North America an interesting pattern shows up in both sets of corrections. Proximate events, in regions well-covered by seismic instrumentation, are corrected large amounts in nearly opposite directions.

4.7 Discussion

A visual comparison of figures 9-11 reveals that models *isc10_direct* and *isc10_sim* are more similar to each other than either of these models is to *isc10_pro*. This observation is confirmed by the correlations in figure 12 and the power distributions in figures 13-19. The simplest interpretation of this result is that the simultaneous inversion has virtually ignored the opportunity to perturb the source parameters, finding it more convenient to absorb the travel time anomalies in to the perturbations in the velocity model. On the other hand, the progressive inversion method projects the maximum amount of the travel time anomaly into the source adjustment, and therefore should have larger source corrections. A comparison of the source correction vectors in figures 20 and 21 confirms this interpretation, with the source corrections emerging from the progressive inversion generally two to four times greater than the simultaneous inversion's corrections.

What is not so obvious is why *isc10_pro* should have more power in the velocity perturbations than the other two models. This difference, as shown in figure 13, is greatest in the shallow mantle, where the sources are located, but continues to exist throughout most of the mantle. Given that more of the travel time anomalies have gone into the source adjustments in the case of the progressive inversion, it might seem that there would be less anomaly left over that could be used to produce velocity perturbations. However, this type of reasoning does not take into account the strong coupling between source mislocations and velocity anomalies. When an earthquake is located assuming a one-dimensional velocity model using travel times that were produced by an earth that contains three-dimensional velocity anomalies, the result in general will not be the true location, but an apparent location which has been adjusted so as to mask the existence of the velocity anomalies. This is particularly true of velocity anomalies in the vicinity of the sources, as the apparent sources will be moved toward regions of increased velocity and away from regions of lower velocity. This masking of velocity anomalies by the source mislocation is apparently quite effective in the case of simultaneous inversion; much of the source mislocation and the velocity anomaly coupled to it are not recognized and, consequently, both of these corrections are underestimated. The advantage of the progressive inversion in this respect is that it operates on the annulled data set which is

independent of the source locations, and thus arrives at velocity anomalies that better represent the actual anomalies. It then takes these velocity anomalies into account in calculating the source corrections, and arrives at more accurate results in this case also. While this explanation does not consider the more complicated effects of incomplete data coverage and the trade-offs between velocity anomalies in different parts of the model, it appears to explain the first-order effects and is consistent with the results of the inversions for both the synthetic and real data. It should be noted here that, based on the results of *O'Connell and Johnson* [1991], the separation of source mislocations and velocity anomalies could be accomplished even more effectively if additional phases, such as pP and S, were included in the data set.

5 Conclusions

From simulations of a global tomographic inversion we discover that when the effects of source mislocation are ignored, velocity anomalies are underestimated by up to 50%, anomalies are smeared into adjacent voxels with values up to 50% of the retrieved velocity of its neighbor, and anomalies are created elsewhere in the mantle with values greater than those estimated for true anomalies. Simultaneous inversion for corrections to the source location and for a velocity model usually improves source locations when initial offsets are "significant" in the sense that ray coverage is distributed in azimuth and distance well enough to constrain the source location to a range smaller than the offset. Velocity estimates are generally accurate, though the magnitudes of the anomalies are less reliable. Also, entirely inaccurate anomalies, produced as artifacts of the inversion, reach disturbingly high values. Progressive inversion improves source locations 60-80% and successfully retrieves velocity anomalies after one iteration for velocity anomalies of 1-2%. The largest ghost image is small compared to the smallest input anomaly.

The success of these tests in correcting the source mislocation and in retrieving the overwhelming portion of the anomalous velocity is probably due to the small source offsets produced by our four velocity anomalies. These small offsets are due, in part, to the relatively good constraints provided by our source-receiver geometry and, in part, to the small number of low-amplitude anomalies introduced to the velocity model. We would expect these results to be even more exaggerated in the real case, in which source mislocations and velocity contrasts are greater than in our simulations. Clearly, careful treatment of the source location problem is critical to the accurate retrieval of three-dimensional velocity variations.

The progressive inversion developed here generally produces more accurate source corrections and velocity anomaly estimates than does an inversion scheme in which both source corrections and velocity terms

are found simultaneously. These results are superior particularly with respect to the suppression of artifact anomalies in the velocity estimation. The source corrections emerging from the progressive inversion are generally two to four times greater than corrections produced by the simultaneous inversion. In the simultaneous case, results are sensitive to the relative scaling of velocity and source terms. With a judicious choice of weights, one could emphasize fitting the source terms at the expense of the fit to the model, but this is not the same as the two-step process followed in the progressive inversion method. In the first case, the simultaneous inversion with hypocentral partial derivatives more heavily weighted than velocity coefficients, the algorithm is still trying to find a best-fitting solution to the two problems at the same time. In the second case, the progressive inversion, the algorithm first uses the portion of the travel time residuals that is independent of source mislocation to determine the velocity terms, and then incorporates this information on 3D velocity structure into the solution for the source mislocation problem.

These results were obtained with tomographic imaging based on raytracing through a one-dimensional velocity model. For larger anomalies, more iterations and three-dimensional raytracing may be necessary. However, computational requirements may not be feasible for such a scheme and better results are not guaranteed. When we perform a second iteration of our algorithms in which the source corrections are applied and rays are calculated from the new locations through the same 1-D model we started with initially, results for both source corrections and velocity terms are mixed. This is probably due to the success of the first iteration. The remaining offsets are small with regard to the standard errors of the first computed source locations.

In our row-active implementation, the progressive inversion scheme used 40% more CPU time than the direct LSQR in vectorized mode. Requirements for disk space (or core memory if the application is small enough to allow the coefficient matrix to be stored in core) is about five times the requirements of the simultaneous inversion. As the projections are performed in the progressive scheme, columns of the previously sparse coefficient matrix are filled in, resulting in a more dense matrix.

As our inversions of real data demonstrate, the two inversion schemes produce clearly different velocity models. Moreover, these differences are concentrated near the models' surfaces, in general, and in source regions, in particular. The bulk of the models' differences are therefore due to the algorithms' differences in their treatment of source terms, and, as the simulations documented in this paper attest, the progressive inversion is more successful at retrieving accurate estimates of velocity anomalies.

Acknowledgments This research was supported by Grants EAR-9105515 and DMS-8810192 of the National Science Foundation and by the Director, Office of Energy Research, Division of Basic Energy Sciences, Engineering, and Geosciences, of the U.S. Department of Energy under contract DE-AC03-76SF00098. Computations were carried out at the Center for Computational Seismology of Lawrence Berkeley Laboratory and at the Statistical Computing Facility, Department of Statistics, UC Berkeley. The authors would like to thank Dan O'Connell and Alberto Michelini for helpful discussions and software.

6 References

Clayton, R.W., and R.P. Comer, A tomographic analysis of mantle heterogeneities from body wave travel times, *EOS Transactions AGU, 64,* 776, 1983.

Dziewonski, A.M., Mapping the lower mantle, Determination of lateral heterogeneity in P velocity up to degree and order 6, *J. Geophys. Res., 89,* 5929–5952, 1984.

Grand, S., Tomographic inversion for shear velocity beneath the North American Plate, *J. Geophys. Res., 92,* 14065–14090, 1987.

Hager, B.H., and R.W. Clayton, Constraints on the structure of mantle convection using seismic observations, flow models, and the geoid, in *Mantle Convection,* W. R. Peltier (Ed.), Gordon and Breach, New York, 657–763, 1989.

van der Hilst, R.D. and E.R. Engdahl, On ISC PP and pP data and their use in delay-time tomography of the Caribbean region. *Geophys. J. Int., 106* 169–188, 1991.

Jeffreys, H., and K.E. Bullen, *Seismological Tables.* British Association for the Advancement of Science, London, 1940.

Jeffreys, H., *The Earth,* Cambridge University Press, London, 1960.

Jordan, T.H., and K.A. Sverdrup, Teleseismic location techniques and their application to earthquake clusters in the South–Central Pacific, *Bull. Seis. Soc. Am., 71,* 1105–1130, 1981.

Kennett, B.L.N., and P.R. Williamson, Subspace methods for large–scale inversion, in *Mathematical Geophysics,* N.J. Vlaar, G. Nolet, M.J.R. Wortel, and S.A.P.L. Cloetingh (eds.), Reidel, Dordrecht, pp. 139–154, 1988.

Lawson, C.L., and R.J. Hanson, *Solving Least Squares Problems.* Prentice–Hall, Englewood Cliffs, N.J., 340 pp., 1974.

Luo, Y., and G.T. Schuster, Wave-equation traveltime inversion, *Geophysics, 56,* 645-653, 1991.

Michelena, R.J., and J.M. Harris, Tomographic traveltime inversion using natural pixels, *Geophysics, 56,* 635–644, 1991.

Morelli, A., and A.M. Dziewonski, Stability of aspherical models of the lower mantle, *EOS Transactions AGU, 66,* 975, 1985.

Morelli, A., and A.M. Dziewonski, 3D structure of the Earth's core inferred from travel–time residuals, *EOS Transactions AGU, 67,* 311, 1986.

Nolet, G., Seismic wave propagation and seismic tomography, in *Seismic Tomography,* G. Nolet (ed.), Reidel, Dordrecht, pp. 1–23, 1987.

Nolet, G., and R. Snieder, Solving large linear inverse problems by projection, *Geophys. Jour. Int., 103,* 565–568, 1990.

O'Connell, D.R.H., Seismic velocity structure and microearthquake source properties at the Geysers, California, geothermal area, *Ph.D. Dissertation,* University of California, Berkeley, 1986.

O'Connell, D.R.H., and L.R. Johnson, Progressive inversion for hypocenters and P wave and S wave velocity structure, Application to the Geysers, California geothermal field, *J. Geophys. Res., 96,* 6223–6236, 1991.

Paige, C. C., and M.A. Saunders, LSQR, An algorithm for sparse linear equations and sparse least squares, *ACM Trans. Math. Software, 8,* 43–71, 198

Pavlis, G.L., and J.R. Booker, The mixed discrete–continuous inverse problem, application to the simultaneous determination of earthquake hypocenters and velocity structure, *J. Geophys. Res., 88,* 4801–4810, 1980.

Pulliam, R.J., and L.R. Johnson, What patterns of heterogeneity in Earth's mantle can be revealed by seismic travel time tomography? *Phys. Earth and Planet. Int.,* in press, March 1992.

Pulliam, R.J., D.W. Vasco, and L.R. Johnson, Tomographic inversions for mantle P-wave velocity structure based on the minimization of l^2 and l^1 norms of ISC travel time residuals, submitted to *J. Geophys. Res.,* March 1992.

Spencer, C., and D. Gubbins, Travel–time inversion for simultaneous earthquake location and velocity structure determination in laterally varying media, *Geophys. J. R. Astron. Soc., 63,* 95–116, 1980.

Stark, P.B., and D.I. Nikolayev, Toward tubular tomography, submitted to *J. Geophys. Res.,* June 1992.

van der Sluis, A., and H.A. van der Vorst, Numerical solution of large, sparse linear systems arising from

tomographic problems, in *Seismic Tomography*, G. Nolet (ed.), Reidel, Dordrecht, pp. 53–87, 1987.

Vasco, D.W., and E.L. Majer, Wavepath traveltime tomography, submitted to *Geophys. J. Int.*, June 1992.

Vasco, D.W., R.J. Pulliam, and L.R. Johnson, Formal inversion of ISC arrival times for mantle P-velocity structure, submitted to *Geophys. J. Int.*, October 1991.

Wielandt, E., On the validity of the ray approximation for interpreting delay times, in *Seismic Tomography*, G. Nolet (ed.), Reidel, Dordrecht, pp. 85–98, 1987.

Woodward, M.J., Wave-equation tomography, *Geophysics, 57*, 15-26, 1992.

7 Appendix: Progressive Inversion

The orthogonal transformation we choose to employ comes from the singular value decomposition (SVD) of the matrix of hypocenter mislocation partial derivatives, **H**. Any matrix may be factored into the form, $\mathbf{H} = \mathbf{U}\mathbf{S}\mathbf{V}^T$ [*Lawson and Hanson*, 1974]. If **H** is an $m \times n$ matrix of rank k, then **U** is an $m \times m$ orthogonal matrix, **V** is an $n \times n$ orthogonal matrix, and **S** is an $m \times n$ diagonal matrix of singular values in which k values are strictly non-zero. The orthogonal matrix $\mathbf{U}^T$ may serve as an annulling transformation matrix, when used to pre-multiply through equation (20). A heuristic proof of this annulling property follows.

Note that only k entries of the diagonal matrix S are non-zero, and that these non-zero elements are all positive. Since

$$\mathbf{H} = \mathbf{U}\mathbf{S}\mathbf{V}^T,$$

then

$$\mathbf{U}^T\mathbf{H} = \mathbf{U}^T\mathbf{U}\mathbf{S}\mathbf{V}^T,$$

$$= \mathbf{S}\mathbf{V}^T,$$

$$= \begin{bmatrix} s_1 & & & 0 \\ & \ddots & & \\ & & s_k & \\ & & 0 & \ddots \\ 0 & & & 0 \end{bmatrix} \mathbf{V}^T.$$

Only the first k rows of $\mathbf{U}^T\mathbf{H}$ contain non-zero elements, therefore only the first k rows will project onto a non-zero (range) space.

By partitioning the data set into individual events and disregarding the station term, equation (20) may be rewritten as

$$\begin{bmatrix} (\delta t)_1 \\ (\delta t)_2 \\ . \\ . \\ . \\ (\delta t)_{n_e} \end{bmatrix} = \begin{bmatrix} \mathbf{H}_1 & 0 & \dots & 0 \\ 0 & \mathbf{H}_2 & \dots & 0 \\ . & 0 & \dots & . \\ . & . & \dots & . \\ . & . & \dots & . \\ 0 & 0 & \dots & \mathbf{H}_{n_e} \end{bmatrix} \begin{bmatrix} (\delta h)_1 \\ (\delta h)_2 \\ . \\ . \\ . \\ (\delta h)_{n_e} \end{bmatrix} + \begin{bmatrix} \mathbf{A}_1 \\ \mathbf{A}_2 \\ . \\ . \\ . \\ \mathbf{A}_{n_e} \end{bmatrix} \boldsymbol{\gamma} \tag{A1}$$

where

$(\delta t)_j \in R^{m_j \times 1}$,

$\mathbf{H}_j \in R^{m_j \times 4}$,

$\delta \mathbf{h}_j \in R^{4 \times 1}$,

$\mathbf{A}_j \in R^{m_j \times n_p}$,

m_j = number of data for the j^{th} event,

$j = 1,2,\dots,n_e$.

The orthogonal transformation matrix now has the form

$$\begin{bmatrix} \begin{bmatrix} \mathbf{U}_R^T \\ \mathbf{U}_N^T \end{bmatrix}_1 & 0 & \dots & 0 \\ 0 & \begin{bmatrix} \mathbf{U}_R^T \\ \mathbf{U}_N^T \end{bmatrix}_2 & \dots & 0 \\ . & 0 & \dots & . \\ . & . & \dots & . \\ . & . & \dots & . \\ 0 & 0 & \dots & \begin{bmatrix} \mathbf{U}_R^T \\ \mathbf{U}_N^T \end{bmatrix}_{n_e} \end{bmatrix}, \tag{A2}$$

where

$(\mathbf{U}_R^T)_j \in R^{4 \times 4}$ = range space of hypocenter partial derivatives for the j^{th} event,

$(\mathbf{U}_N^T)_j \in R^{(m_j - 4) \times 4}$ = null space of hypocenter partial derivatives for the j^{th} event,

$j = 1,2,...,n_e$.

Applying the transformation matrix (A2) to equation (A1) we get

$$\begin{bmatrix} \begin{bmatrix} \delta \mathbf{t}_R \\ \delta \mathbf{t}_N \end{bmatrix}_1 \\ \begin{bmatrix} \delta \mathbf{t}_R \\ \delta \mathbf{t}_N \end{bmatrix}_2 \\ \vdots \\ \begin{bmatrix} \delta \mathbf{t}_R \\ \delta \mathbf{t}_N \end{bmatrix}_{n_e} \end{bmatrix} = \begin{bmatrix} \begin{bmatrix} \mathbf{H}_R \\ 0 \end{bmatrix}_1 & 0 & \cdots & 0 \\ 0 & \begin{bmatrix} \mathbf{H}_R \\ 0 \end{bmatrix}_2 & \cdots & 0 \\ \vdots & \vdots & \ddots & \vdots \\ 0 & 0 & \cdots & \begin{bmatrix} \mathbf{H}_R \\ 0 \end{bmatrix}_{n_e} \end{bmatrix} \begin{bmatrix} \delta h_1 \\ \delta h_2 \\ \vdots \\ \delta h_{n_e} \end{bmatrix} + \begin{bmatrix} \begin{bmatrix} \mathbf{A}_R \\ \mathbf{A}_N \end{bmatrix}_1 \\ \begin{bmatrix} \mathbf{A}_R \\ \mathbf{A}_N \end{bmatrix}_2 \\ \vdots \\ \begin{bmatrix} \mathbf{A}_R \\ \mathbf{A}_N \end{bmatrix}_{n_e} \end{bmatrix} \boldsymbol{\gamma}, \tag{A3}$$

where

$(\delta \mathbf{t}_R)_j = (\mathbf{U}_R^T)_j \delta t \in R^{4\times 1}$ = travel time residual in range space of hypocenter partial derivatives,

$(\mathbf{H}_R)_j = (\mathbf{U}_R^T)_j \mathbf{H}_j \in R^{4\times 4}$ = rotated matrix of hypocenter mislocation partial derivatives,

$\delta \mathbf{h}_j \in R^{4\times 4}$ = matrix of hypocenter mislocation partial derivatives for event i,

$(\mathbf{A}_R)_j = (\mathbf{U}_R^T)_j \mathbf{A}_j \in R^{4\times n_p}$ = portion of rotated $\mathbf{A}$ that contributes to $\delta \mathbf{t}_R$,

$(\delta \mathbf{t}_N)_j = (\mathbf{U}_N^T)_j \delta t \in R^{(m_j-4)\times 4}$ = travel time residual in null space of hypocenter partial derivatives,

$(\mathbf{A}_N)_j = (\mathbf{U}_N^T)_j \mathbf{A}_j \in R^{4\times n_p}$ = portion of rotated $\mathbf{A}$ that contributes only to $\delta \mathbf{t}_N$,

$j = 1,2,...,n_e$.

Rearranging (A3) gives

$$\begin{bmatrix} (\delta t_R)_1 \\ (\delta t_R)_2 \\ \cdot \\ \cdot \\ \cdot \\ (\delta t_R)_{n_e} \\ - \\ (\delta t_N)_1 \\ (\delta t_N)_2 \\ \cdot \\ \cdot \\ \cdot \\ (\delta t_N)_{n_e} \end{bmatrix} = \begin{bmatrix} (\mathbf{H}_R)_1 & 0 & \cdots & 0 \\ 0 & (\mathbf{H}_R)_2 & \cdots & 0 \\ \cdot & 0 & \cdots & \cdot \\ \cdot & \cdot & \cdots & \cdot \\ \cdot & \cdot & \cdots & \cdot \\ 0 & 0 & \cdots & (\mathbf{H}_R)_{n_e} \\ - & - & - & - \\ 0 & 0 & \cdots & 0 \\ 0 & 0 & \cdots & 0 \\ \cdot & \cdot & \cdots & \cdot \\ \cdot & \cdot & \cdots & \cdot \\ \cdot & \cdot & \cdots & \cdot \\ 0 & 0 & \cdots & 0 \end{bmatrix} \begin{bmatrix} \delta h_1 \\ \delta h_2 \\ \cdot \\ \cdot \\ \cdot \\ \delta h_{n_e} \end{bmatrix} + \begin{bmatrix} (\mathbf{A}_R)_1 \\ (\mathbf{A}_R)_2 \\ \cdot \\ \cdot \\ \cdot \\ (\mathbf{A}_R)_{n_e} \\ - \\ (\mathbf{A}_N)_1 \\ (\mathbf{A}_N)_2 \\ \cdot \\ \cdot \\ \cdot \\ (\mathbf{A}_N)_{n_e} \end{bmatrix} \boldsymbol{\gamma}. \tag{A4}$$

We may now separate the two problems

$$\boldsymbol{\delta t}_R = \mathbf{H}_R \ \boldsymbol{\delta h} \ + \mathbf{A}_R \ \boldsymbol{\gamma}, \tag{A5}$$

and

$$\boldsymbol{\delta t}_N = \mathbf{A}_N \ \boldsymbol{\gamma}, \tag{A6}$$

where

$\boldsymbol{\delta t}_R \in R^{4n_e \times 1}$,

$\mathbf{H}_R \in R^{4n_e \times 4n_e}$,

$\boldsymbol{\delta h} \in R^{4n_e \times 4}$,

$\mathbf{A}_R \in R^{4n_e \times n_p}$,

$\boldsymbol{\delta t}_N \in R^{m \times 1}$,

$\mathbf{A}_N \in R^{m \times n_p}$,

$m = M - 4n_e$ = (total number of data) - 4 × (the number of events).

For an individual event, equation (A5) becomes

$$(\boldsymbol{\delta t}_R)_j = (\mathbf{H}_R)_j \ (\boldsymbol{\delta h})_j + (\mathbf{A}_R)_j \ \boldsymbol{\gamma}, \tag{A7}$$

where

$$(\delta \mathbf{t}_R)_j \in R^{4\times 1},$$

$$(\mathbf{H}_R)_j \in R^{4\times 4},$$

$$(\delta \mathbf{h})_j \in R^{4\times 1},$$

$$(\mathbf{A}_R)_j \in R^{4\times n_p},$$

$$j = 1,2,\ldots,n_e .$$

Equation (A6) is independent of hypocenter mislocation, $\delta\mathbf{h}$. We solve it first, then use the solution obtained for γ to substitute into equation (A7) for all events and solve for $(\delta\mathbf{h})_j$, j=1,n_e.

8 List of Tables

Table 1 The source corrections resulting from the simultaneous and progressive inversions for Event 1, located under the Kamchatka Peninsula. For each source parameter the first column indicates the "a priori" standard error. This is the standard error from the initial location of the sources introduced into the JB model and located in the JB model with no anomalies present. These standard errors represent the best any algorithm can hope to achieve with the given ray coverage. The second column contains the initial parameter offset. For each parameter, these are the amounts the sources re-located in the 3-D model differ from the true source locations. Column three contains the results after source corrections obtained from the simultaneous inversion have been applied to the initial parameter offset and it shows how far away the corrected source are from the true sources. The next column shows how much the simultaneous inversion improved the source locations. Columns five and six contain information similar to columns three and four, but for corrections that emerge from the progressive inversion.

Table 2 The information contained in Table 2 is similar to the information contained in Table 1, but for Event 2, located in the Chilean Subduction Zone.

Table 3 The information contained in Table 3 is similar to the information contained in Table 1, but for Event 3, located in the Mariana Subduction Zone.

Table 4 The information contained in Table 4 is similar to the information contained in Table 1, but for Event 4, located in Mongolia, China.

Table 5 The information contained in Table 5 is similar to the information contained in Table 1, but for Event 5, located in the Aleutian Islands.

Table 6 The information contained in Table 6 is similar to the information contained in Table 1, but for Event 6, located in the Central American Subduction Zone.

Table 7 The information contained in Table 7 is similar to the information contained in Table 1, but for Event 7, located in the South China Sea.

Table 8 The information contained in Table 8 is similar to the information contained in Table 1, but for Event 8, located in the Himalayas.

Table 9 The information contained in Table 9 is similar to the information contained in Table 1, but for Event 9, located in the South Pacific Ocean.

Table 10 Estimates for the four input anomalies and a fifth entry for the next largest value emerging from the inversion. This fifth entry is the largest artifact anomaly and does not represent the same voxel across the bottom row of the table. Column 2 shows the number of rays visiting each anomalous block. We place a "peak" anomaly at the center point of a voxel and constrain the anomaly to decrease linearly toward the voxel's boundaries. To find the actual image we are trying to recover, neglecting the effects of imperfect ray coverage, we invert residuals calculated by subtracting the synthetic travel times from travel times through the JB model from the *true* source locations. This result is listed in column 4. Columns 5 and 6 show the results of directly inverting the data from mislocated sources. Columns 7 and 8 show the same information for the simultaneous estimation of source and velocity terms. The last two columns show the results of our progressive inversion scheme.

Table 11 Details of the model parametrization and the sampling provided by our data set. Include are the average number of hits for sampled voxels in each layer along with the the average sum of ray segments in a voxel at a given depth and the number of voxels sampled in each depth interval. These averages include only voxels that have non-zero sampling.

9 List of Figures

Figure 1 Flow chart outlining the steps performed in the tomography simulations.

Figure 2 Locations of sources (large gray spheres) and stations (small black dots) used to construct the synthetic data set for the simulations. The data set consists of 9 events and a total of 207 stations. An average of 45 arrivals are calculated for each event.

Figure 3 a) Model parametrization and input anomalies for layer 2: 483-966 km. The model mantle is parametrized as voxels, 30° × 30° at the equator and 500 km thick, for a total of 276 model parameters. Voxels in a given layer have approximately equal surface area. The introduced velocity anomalies are highlighted in white (–0.20 *km/s*) and black (0.15 *km/s*). b) Input anomalies for layer 3, 966-1449 km depth, are 0.30 *km/s* and 0.10 *km/s*.

Figure 4 (a-f) Ray coverage of the mantle is indicated in terms of the number of rays that sample each voxel. The most-sampled voxel has 96 hits; several voxels has more than 72 hits. All six depth layers of our model are shown: (a) 0-483 km, (b) 483-966 km, (c) 966-1449 km, (d) 1449-1932 km, (e) 1932-2415 km, (f) 2415-2898 km.

Figure 5 a) Locations of sources used in the inversions of real data. The data set consists of about 3,000 shallow events located by the ISC for the time period January 1964 - January 1987. A minimum of forty observations was required to include an event. b) Locations of seismographic stations that reported the observations used in this study.

Figure 6 Histogram of the nearly 345,000 travel time residuals associated with the events included in this study, Source depths are greater than 0 km and less than 70 km. Also shown are the first four moments of the distribution.

Figure 7 The model mantle is parametrized as voxels, 10° × 10° at the equator and generally 200 km thick, for a total of 5684 model parameters. Voxels in a given layer have approximately equal surface area.

Figure 8 (a-h) Ray coverage of the mantle provided by the approximately 345,000 observations included in our data set is shown in terms of the number of rays that sample each voxel, The most-sampled voxel has over 50,000 samples. Only 166 of 5684 voxels are unsampled. The layers shown are: (a) 0-200 km, (b) 200-400 km, (c) 400-670 km, (d) 670-870 km, (e) 1270-1470 km, (f) 1470-1670 km, (g) 2470-2670 km, and (h) 2670-2898 km.

Figure 9 (a-f) Six depth layers of model *isc10_direct*, the direct inversion that neglects source terms: (a) 0-200 km, (b) 200-400 km, (c) 400-670 km, (d) 1270-1470 km, (e) 1470-1670 km, and (f) 2470-2670 km.

Figure 10 (a-f) Six depth layers of model *isc10_sim*, the simultaneous inversion for both source and velocity terms. The layers shown are the same as in figure 9.

Figure 11 (a-f) Six depth layers of model *isc10_pro*, the progressive inversion for source and velocity terms in succession. The layers shown are the same as in figure 9.

Figure 12 The Spearman rank-order correlations between layers of each set of two models as functions of depth. When comparing a given layer of two models we replace each velocity value from the first model with its rank among the $N-1$ other values in the same layer, and do likewise with values from the same layer of the second model. This statistic allows us to examine correlations between small-scale features of the models. The significance level comes from a Student's t distribution with N-1 degrees of freedom.

Figure 13 Power contained in surface spherical harmonic series expansions of the three velocity models as a function of depth.

Figure 14 Power in the spherical harmonic expansions for each depth interval of model *isc10_direct* as a function of angular degree. All values are normalized to the maximum value appearing in the figure. Numbers on the right refer to the maximum power for each layer.

Figure 15 Power in the spherical harmonic expansions for each depth interval of model *isc10_sim* as a function of angular degree. Conventions are the same as in figure 14.

Figure 16 Power in the spherical harmonic expansions for each depth interval of model *isc10_pro* as a function of angular degree. Conventions are the same as in figure 14.

Figure 17 Power in spherical harmonic series generated by averaging *isc10_direct* layer expansions through the whole mantle and through the upper and lower mantle separately. Conventions are the same as in figure 14.

Figure 18 Power in spherical harmonic series generated by averaging *isc10_sim* layer expansions through the whole mantle and through the upper and lower mantle separately. Conventions are the same as in figure 14.

Figure 19 Power in spherical harmonic series generated by averaging *isc10_pro* layer expansions through the whole mantle and through the upper and lower mantle separately. Conventions are the same as in figure 14.

Figure 20 Source correction vectors produced by the simultaneous inversion for 400 of the 3077 events used in this study. In each case the starting location is indicated with either an asterisk or hexagon and a scaled vector points in the direction of the correction required by the latitude and longitude adjustments. For each event the direction of the depth correction is indicated by the type of symbol marking the relocation vector's endpoint. Size of the depth correction is indicated by the size of the symbol. Events that require a shallowing correction are marked with asterisks; events that are relocated deeper are marked by a hexagon. Origin time corrections are not shown. Both figures 20 and 21 are scaled to the same maximum vector length.

Figure 21 Source correction vectors produced by the progressive inversion for the same 400 events shown in figure 20. Conventions are the same as for figure 20.

Event 1: Kamchatka Peninsula (53.0°N, 160.0°E, 73.9 km)

Table 1

Source parameter	"a priori" standard error	Initial parameter offset	After correction: Simultaneous parameter offset	Simultaneous % improved	Progressive parameter offset	Progressive % improved
origin time (sec)	0.00	0.00	-0.08		0.04	
latitude (deg)	0.163	-0.008	0.003	63%	0.002	77%
longitude (deg)	0.420	-0.080	-0.008	90%	-0.034	58%
depth (km)	0.329	2.70	-0.75	72%	0.07	97%

Event 2: South American Subduction Zone (31.1°S, 67.9°W, 72.2 km)

Table 2

Source parameter	"a priori" standard error	Initial parameter offset	After correction: Simultaneous parameter offset	Simultaneous % improved	Progressive parameter offset	Progressive % improved
origin time (sec)	0.14	0.00	-0.09		0.00	
latitude (deg)	0.022	-0.006	0.004	33%	0.002	75%
longitude (deg)	0.029	0.006	0.004	33%	0.001	90%
depth (km)	0.18	0.10	1.00	-900%	0.16	-67%

Event 3: Mariana Subduction Zone (18.9°N, 144.8°E, 41.0 km)

Table 3

Source parameter	"a priori" standard error	Initial parameter offset	After correction: Simultaneous parameter offset	Simultaneous % improved	Progressive parameter offset	Progressive % improved
origin time (sec)	0.26	0.18	-0.03	83%	0.01	92%
latitude (deg)	0.019	0.031	-0.024	23%	0.003	92%
longitude (deg)	0.015	-0.012	-0.001	92%	0.001	90%
depth (km)	2.82	0.30	1.75	-483%	0.55	-85%

Event 4: Mongolia
(50.0°N, 110.0°E, 180.0 km)

Table 4

Source parameter	"a priori" standard error	Initial parameter offset	After correction: Simultaneous parameter offset	Simultaneous % improved	Progressive parameter offset	Progressive % improved
origin time (sec)	0.00	-0.05	-0.02	60%	0.00	100%
latitude (deg)	0.031	0.005	0.003	40%	0.001	80%
longitude (deg)	0.047	0.041	0.015	63%	0.016	61%
depth (km)	0.31	8.70	4.58	47%	0.01	100%

Event 5: Aleutian Islands
(51.0°N, 178.0°W, 50.0 km)

Table 5

Source parameter	"a priori" standard error	Initial parameter offset	After correction: Simultaneous parameter offset	Simultaneous % improved	Progressive parameter offset	Progressive % improved
origin time (sec)	0.69	2.09	2.04	2%	0.08	96%
latitude (deg)	0.024	0.024	-0.005	79%	-0.006	74%
longitude (deg)	0.036	-0.159	-0.022	86%	-0.066	58%
depth (km)	6.57	24.30	23.81	2%	0.55	98%

Event 6: Central American Subduction Zone
(9.5°N, 84.1°W, 66.6 km)

Table 6

Source parameter	"a priori" standard error	Initial parameter offset	After correction: Simultaneous parameter offset	Simultaneous % improved	Progressive parameter offset	Progressive % improved
origin time (sec)	0.23	0.00	0.15		0.09	
latitude (deg)	0.013	-0.023	-0.017	26%	-0.009	63%
longitude (deg)	0.014	-0.012	0.024	-100%	0.003	76%
depth (km)	2.52	-3.10	-0.71	77%	-1.46	53%

Event 7: South China Sea
(18.8°N, 111.9°, 53.0 km)

Table 7

Source parameter	"a priori" standard error	Initial parameter offset	After correction: Simultaneous parameter offset	Simultaneous % improved	Progressive parameter offset	Progressive % improved
origin time (sec)	0.12	-0.01	-0.13	-1200%	-0.10	-900%
latitude (deg)	0.208	0.029	0.01	66%	0.003	90%
longitude (deg)	0.228	0.010	0.003	70%	0.004	63%
depth (km)	15.84	2.50	0.46	82%	1.30	48%

Event 8: Himalayas
(30.5°N, 79.4°E, 88.0 km)

Table 8

Source parameter	"a priori" standard error	Initial parameter offset	After correction: Simultaneous parameter offset	Simultaneous % improved	Progressive parameter offset	Progressive % improved
origin time (sec)	0.28	-0.12	-0.05	42%	-0.06	50%
latitude (deg)	0.022	0.022	0.004	82%	0.000	100%
longitude (deg)	0.027	0.038	0.084	-120%	0.011	71%
depth (km)	2.84	0.20	1.45	-625%	-0.13	36%

Event 9: South Pacific
(20.8 126.9°W, 87.8 km)

Table 9

Source parameter	"a priori" standard error	Initial parameter offset	After correction: Simultaneous parameter offset	Simultaneous % improved	Progressive parameter offset	Progressive % improved
origin time (sec)	0.45	0.00	-0.08		-0.01	
latitude (deg)	0.022	0.001	0.061	-6000%	-0.002	-50%
longitude (deg)	0.020	-0.007	0.005	29%	0.001	80%
depth (km)	4.33	0.60	0.12	80%	0.23	61%

Velocity Anomalies

Table 10

			Inversions						
			No source offset	With source offset					
				Direct		Simultaneous		Progressive	
anomaly	# hits	peak	km/sec	km/sec	%	km/sec	%	km/sec	
1	18	0.100	0.063	0.038	60%	0.066	105%	0.064	101%
2	56	0.300	0.187	0.168	90%	0.170	91%	0.184	98%
3	72	0.150	0.079	0.036	46%	0.087	110%	0.079	100%
4	38	-0.200	-0.088	-0.058	66%	-0.055	63%	-0.080	91%
next		0.000	0.010	-0.042		0.051		0.017	

Table 11: Model layer depths and average voxel sampling

Layer number	Depth range (km)	Average velocity (km/s)	Average voxel volume (10^8 km^3)	Number of voxels sampled	% of voxels sampled	Average number hits	Average column sum of A (10^4 km)
1	0-200	7.94	2.43	333	82	2375	51.25
2	200-400	8.58	2.28	352	87	2122	47.66
3	400-670	9.88	2.85	383	94	2115	66.96
4	670-870	10.95	1.94	394	97	1900	53.72
5	870-1070	11.40	1.81	402	99	1712	51.23
6	1070-1270	11.68	1.67	406	100	1460	42.23
7	1270-1470	11.96	1.55	406	100	1293	37.54
8	1470-1670	12.24	1.43	406	100	1134	32.74
9	1670-1870	12.51	1.31	406	100	1008	29.31
10	1870-2070	12.76	1.20	406	100	908	27.19
11	2070-2270	13.01	1.09	406	100	768	24.22
12	2270-2470	13.24	0.99	406	100	587	18.75
13	2470-2670	13.47	0.89	406	100	430	14.64
14	2670-2898	13.64	0.91	406	100	164	5.78

fig. 1

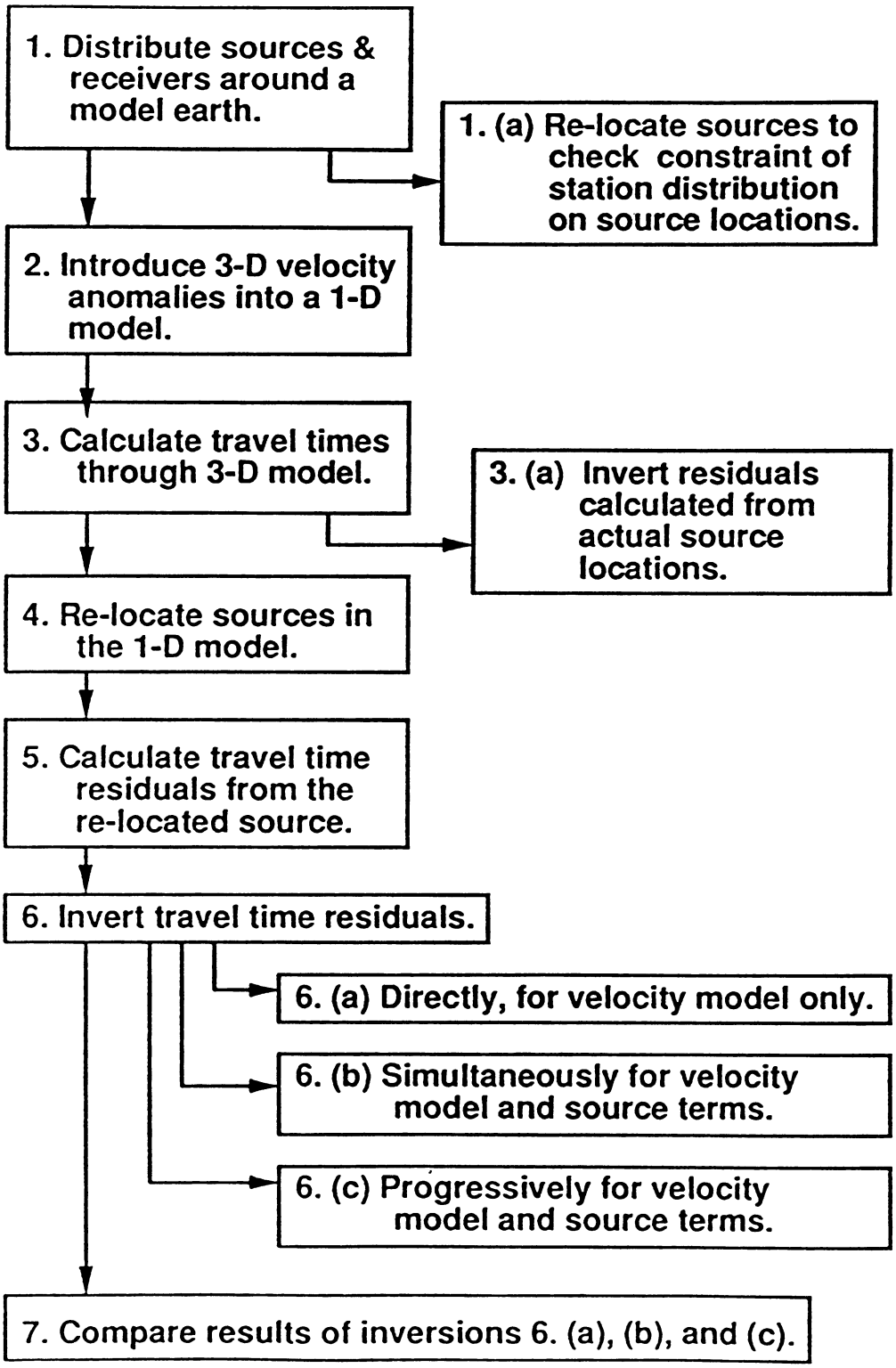
1. Distribute sources & receivers around a model earth.
1. (a) Re-locate sources to check constraint of station distribution on source locations.
2. Introduce 3-D velocity anomalies into a 1-D model.
3. Calculate travel times through 3-D model.
3. (a) Invert residuals calculated from actual source locations.
4. Re-locate sources in the 1-D model.
5. Calculate travel time residuals from the re-located source.
6. Invert travel time residuals.
6. (a) Directly, for velocity model only.
6. (b) Simultaneously for velocity model and source terms.
6. (c) Progressively for velocity model and source terms.
7. Compare results of inversions 6. (a), (b), and (c).

fig. 2

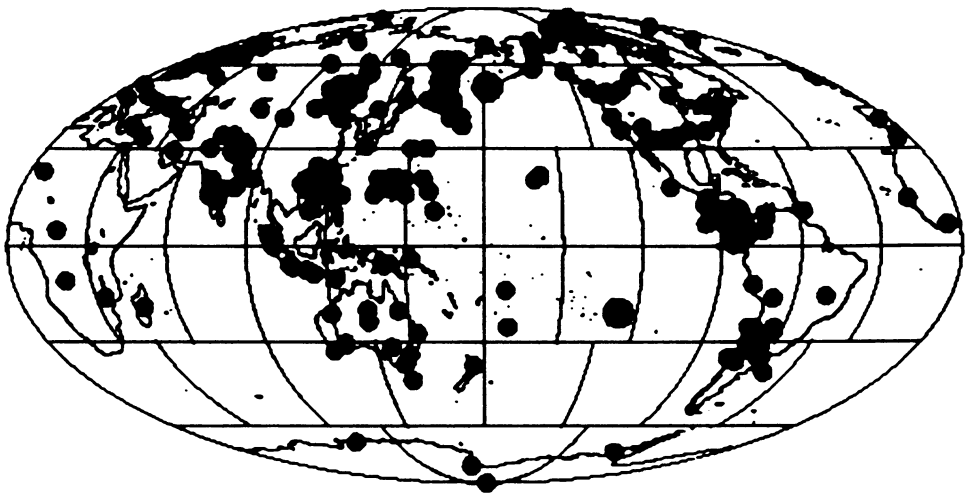

fig. 3a

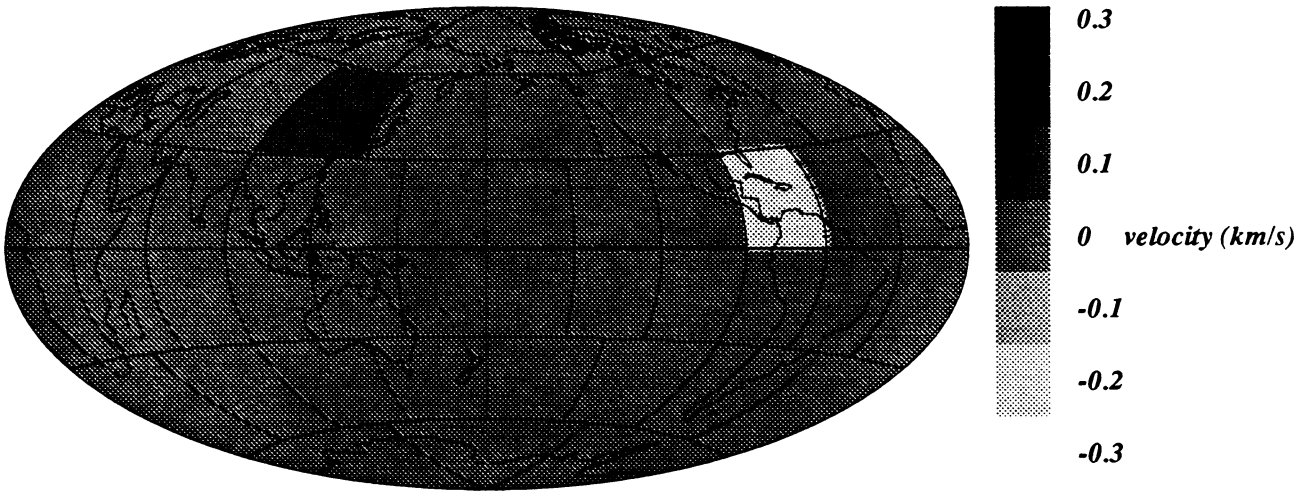

Input anomalies, layer 2

fig. 3b

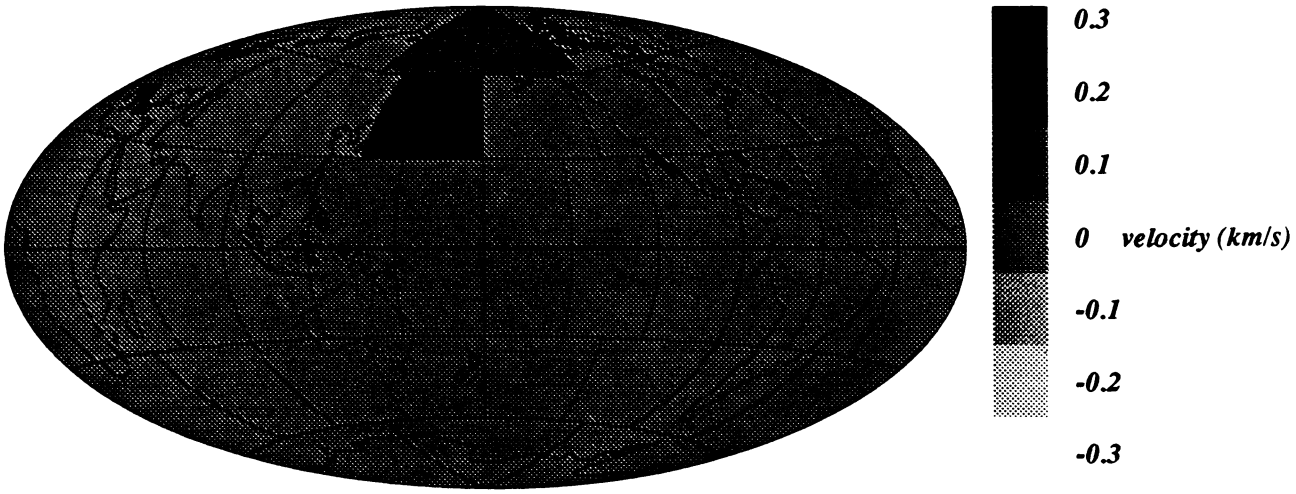

Input anomalies, layer 3

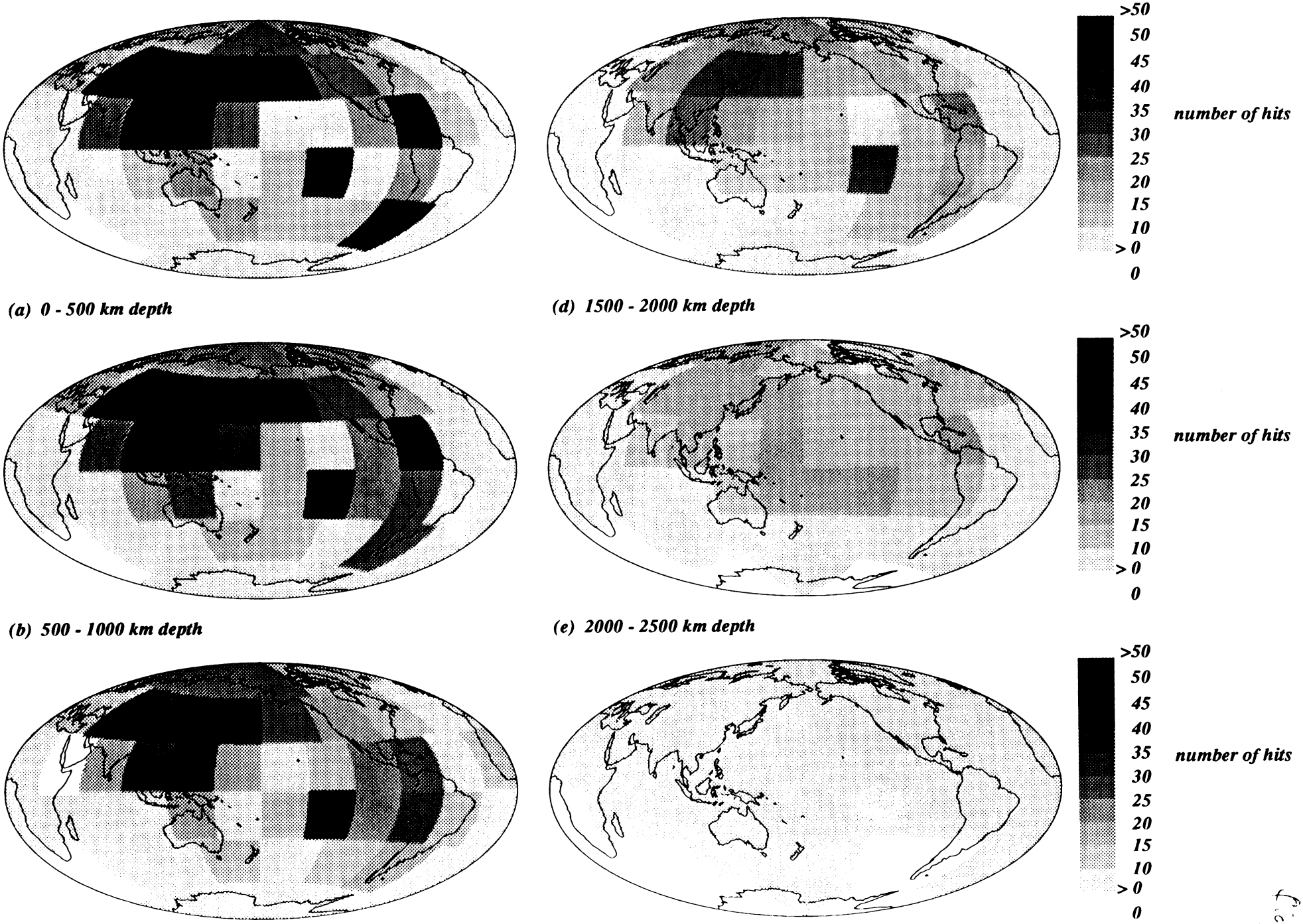

(a) 0 - 500 km depth

(b) 500 - 1000 km depth

(c) 1000 - 1500 km depth

(d) 1500 - 2000 km depth

(e) 2000 - 2500 km depth

(f) 2500 km - CMB

fig. 5

fig. 5(a)

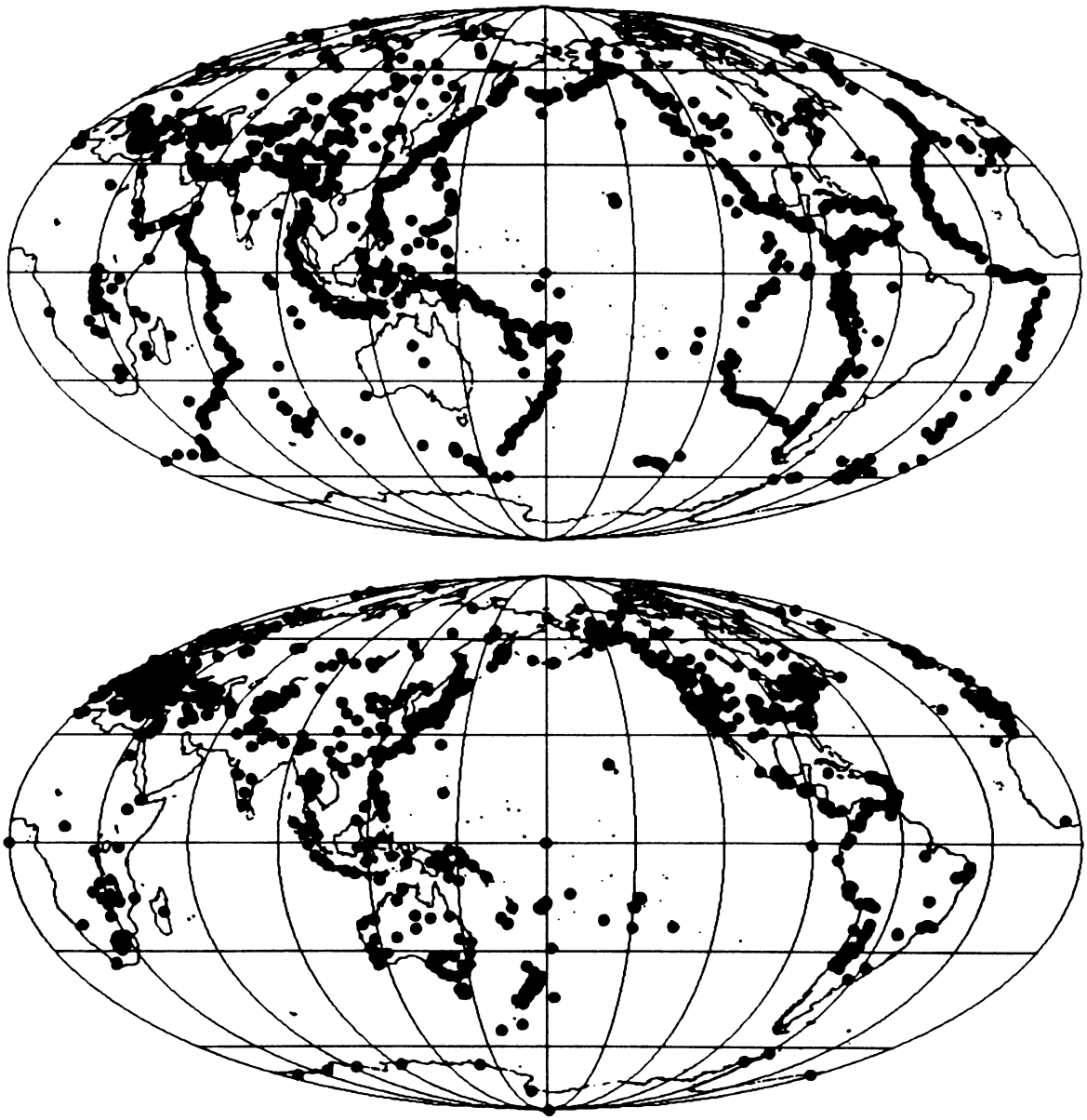

fig. 5 (b)

fig. 6

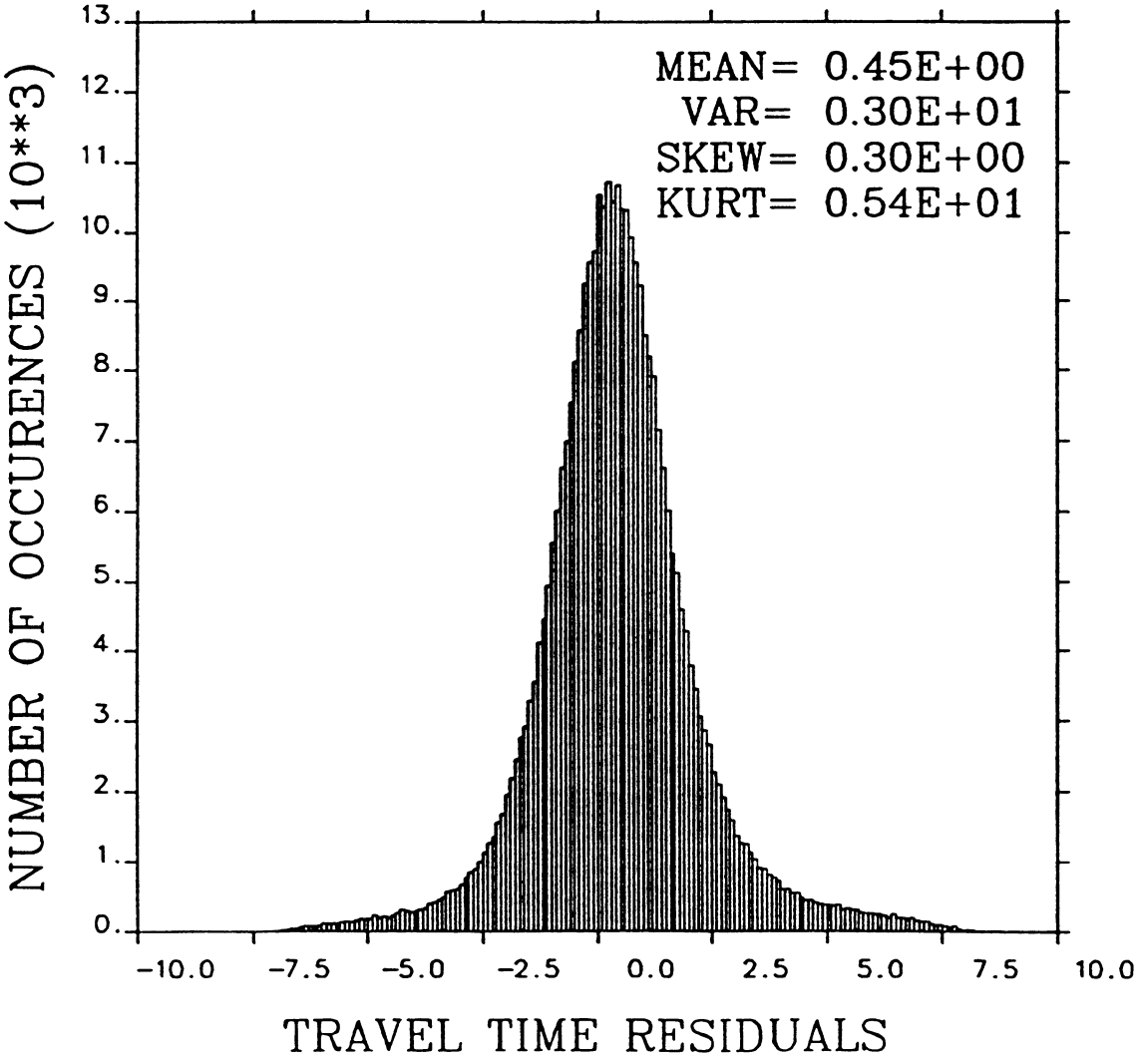
MEAN= 0.45E+00
VAR= 0.30E+01
SKEW= 0.30E+00
KURT= 0.54E+01
NUMBER OF OCCURENCES (10**3)
13.
12.
11.
10.
9.
8.
7.
6.
5.
4.
3.
2.
1.
0.
-10.0
-7.5
-5.0
-2.5
0.0
2.5
5.0
7.5
10.0
TRAVEL TIME RESIDUALS

fig 7

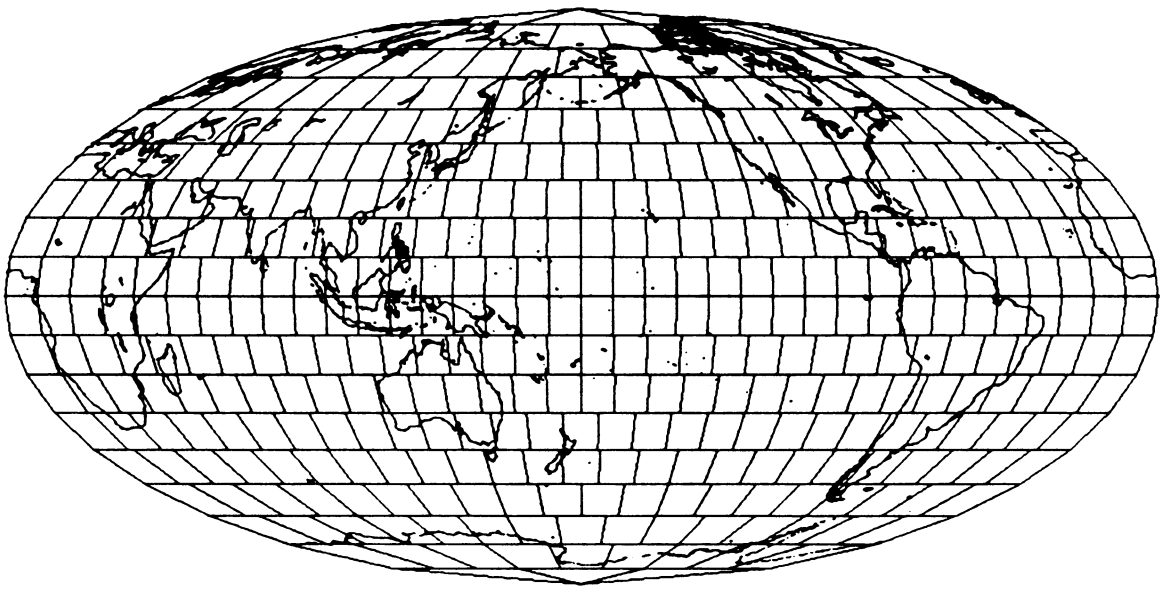

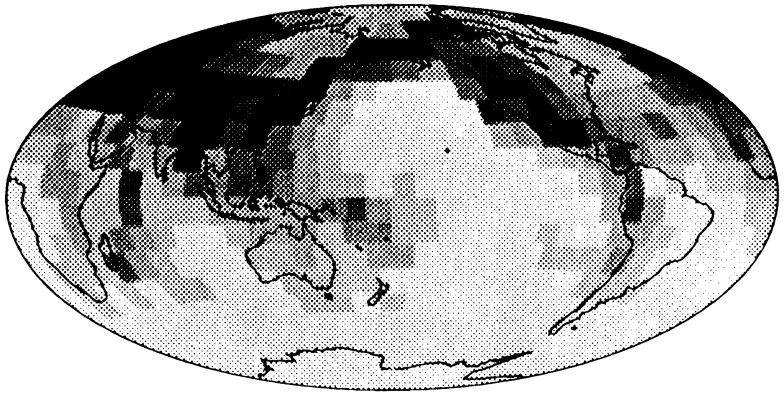

(e) 1270 - 1470 km depth

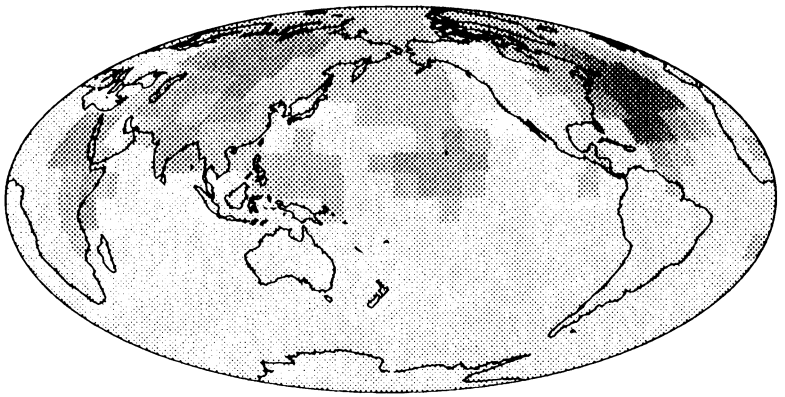

(g) 2470 - 2670 km depth

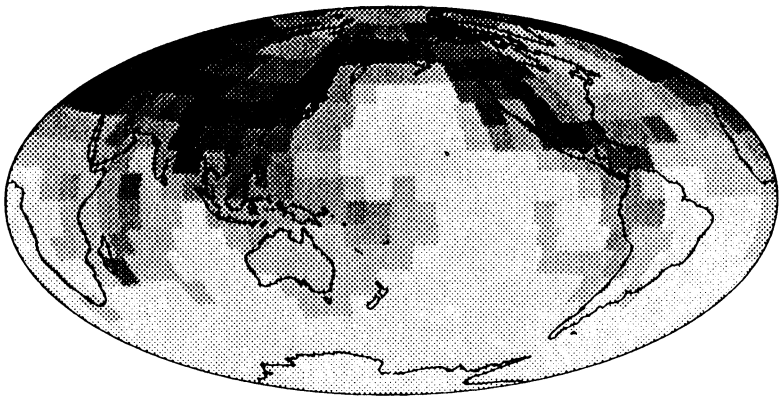

(f) 1470 - 1670 km depth

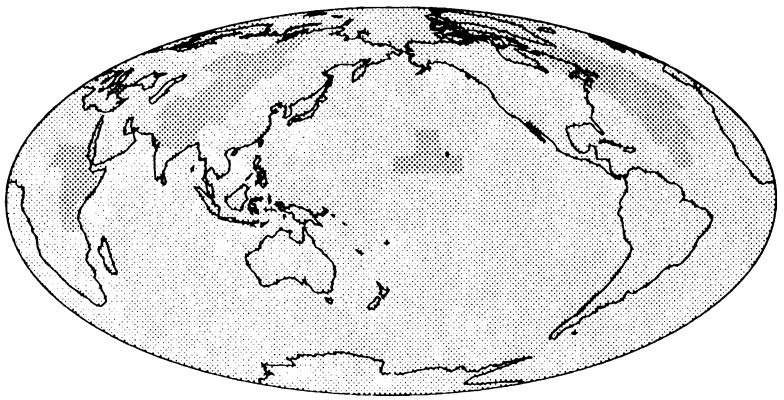

(h) 2670 km - CMB

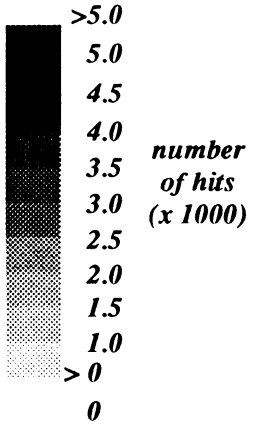

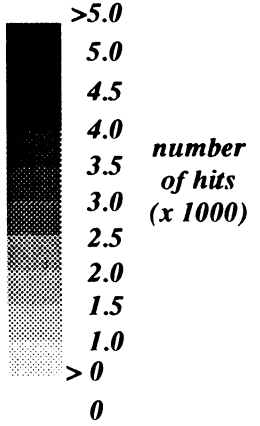

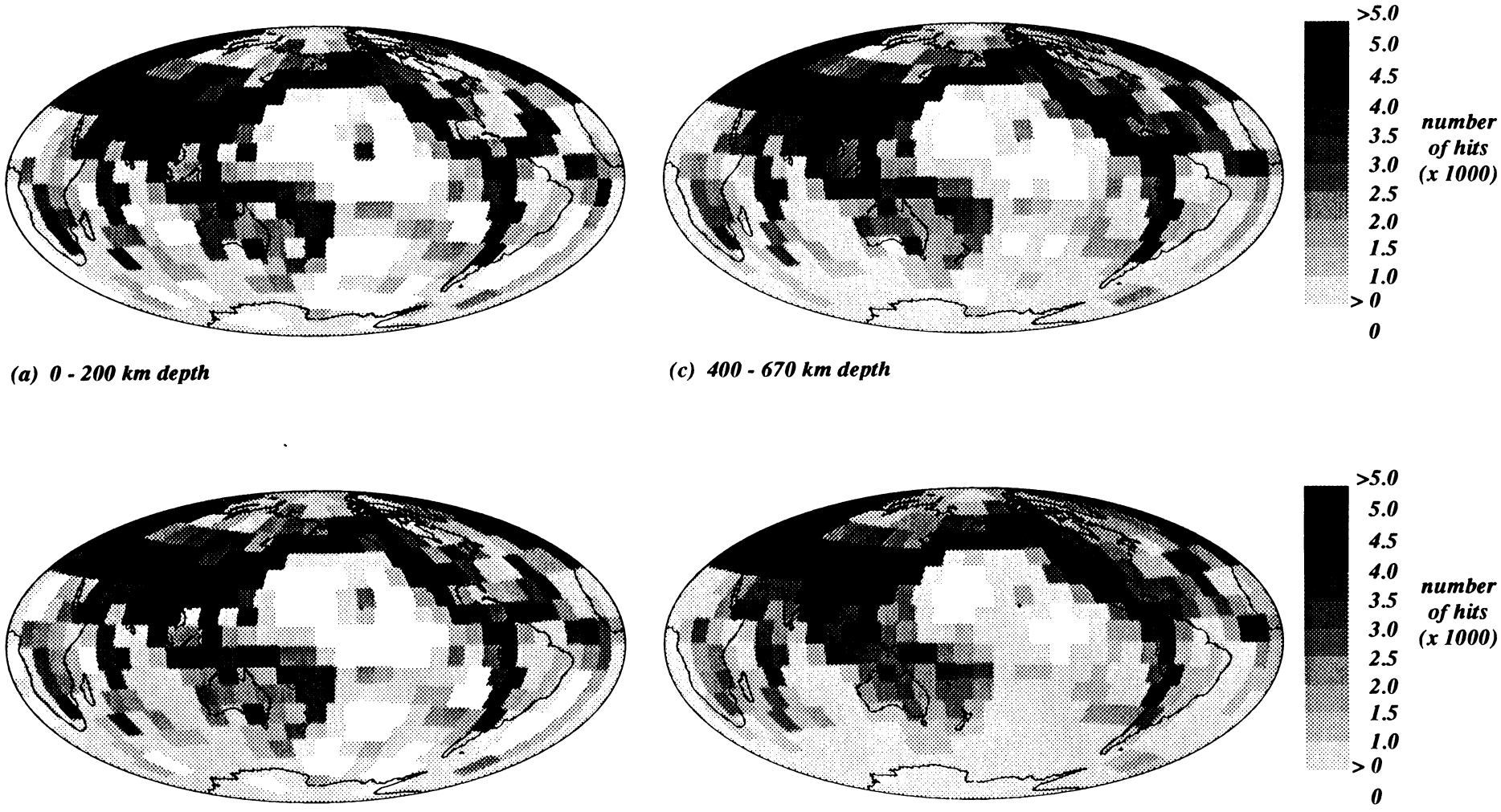

(a) 0 - 200 km depth

(c) 400 - 670 km depth

(b) 200 - 400 km depth

(d) 670 - 870 km depth

Fig 8

Model isc10_direct

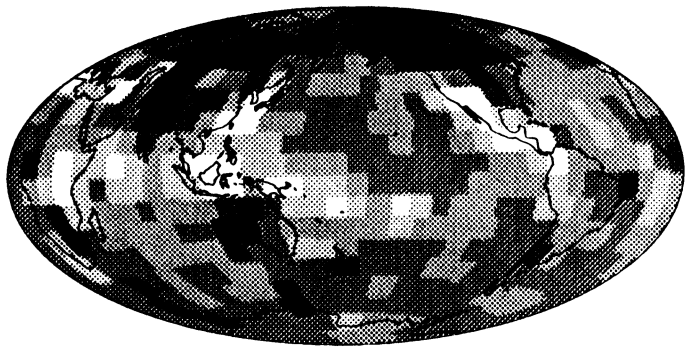

(a) 0 - 200 km depth

(b) 200 - 400 km depth

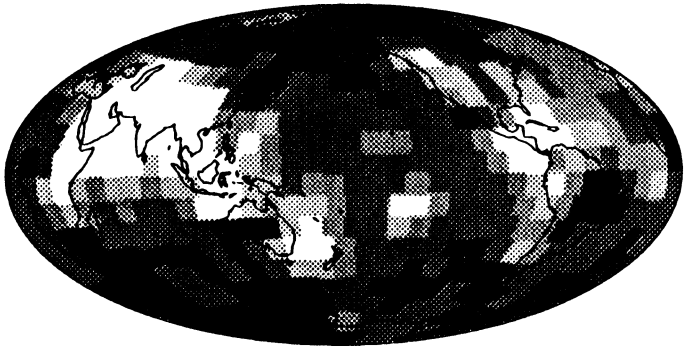

(c) 400 - 670 km depth

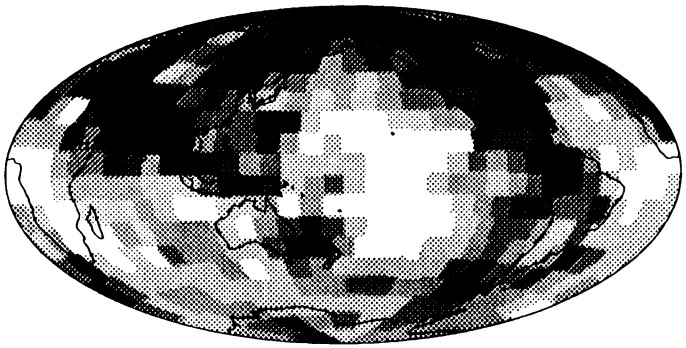

(d) 1270 - 1470 km depth

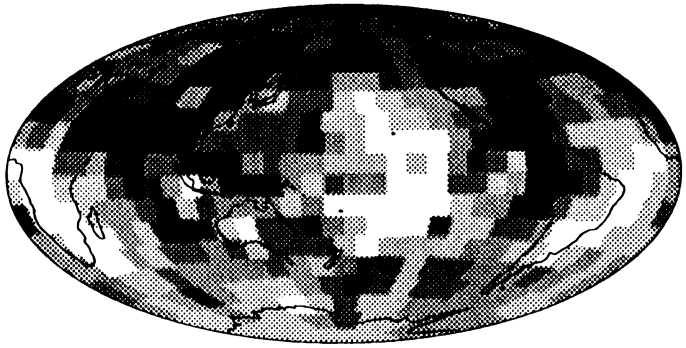

(e) 1470 - 1670 km depth

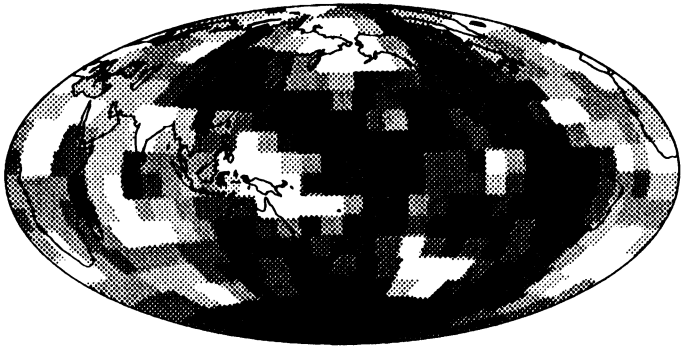

(f) 2470 - 2670 km depth

Fig. 9

Model isc10_sim

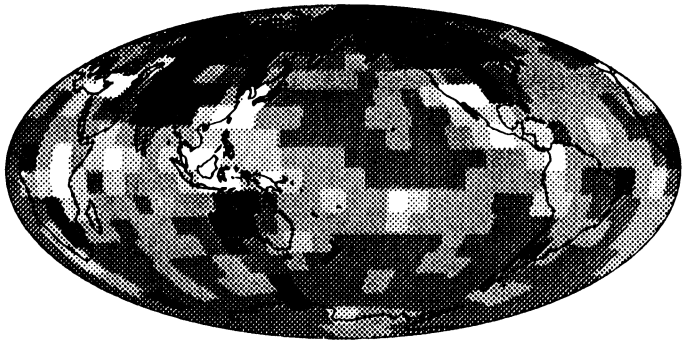

(a) 0 - 200 km depth

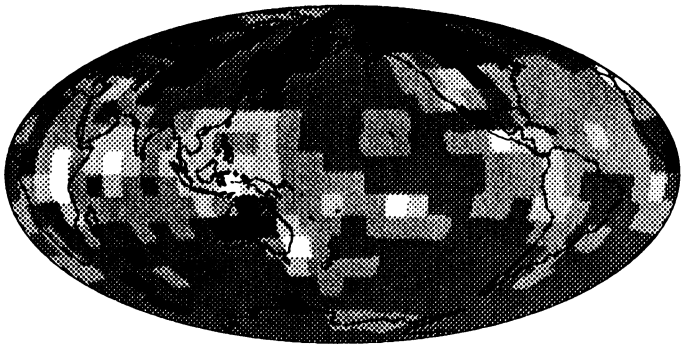

(b) 200 - 400 km depth

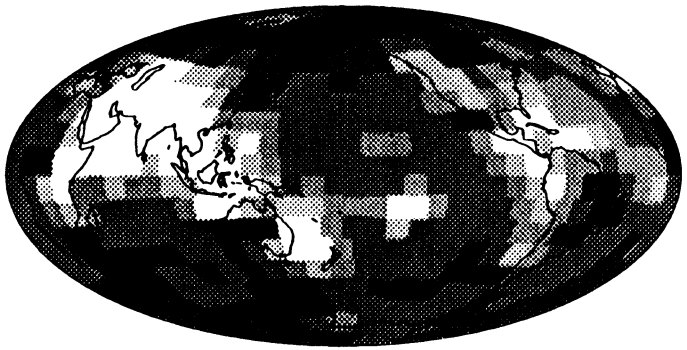

(c) 400 - 670 km depth

velocity (%)

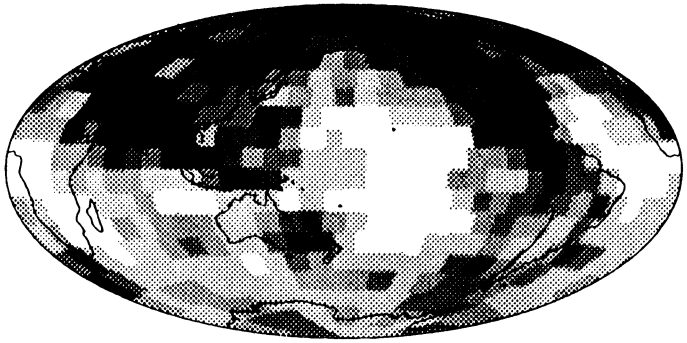

(d) 1270 - 1470 km depth

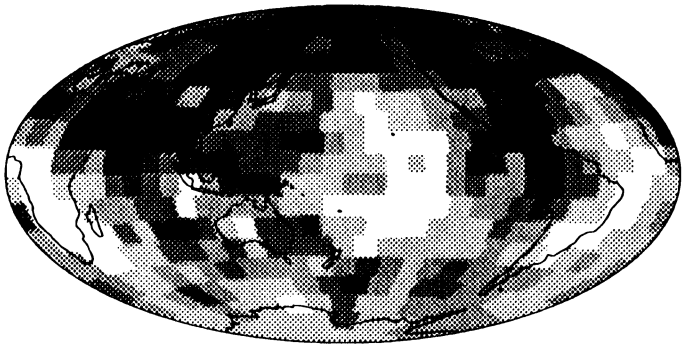

(e) 1470 - 1670 km depth

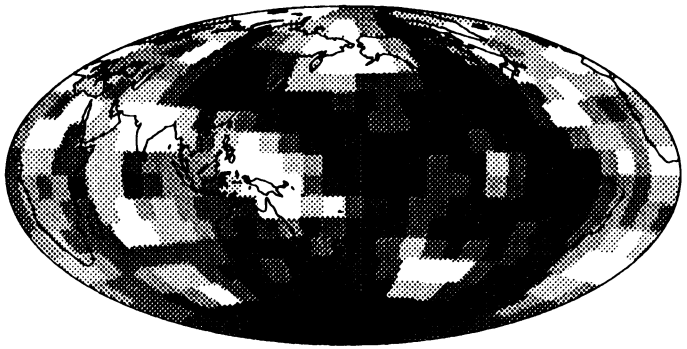

(f) 2470 - 2670 km depth

velocity (%)

fig 10

Model isc10_pro

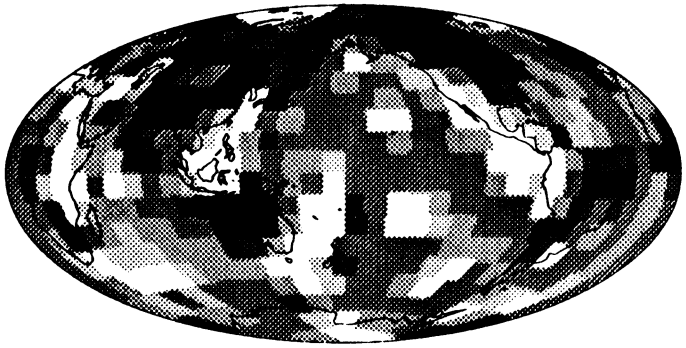

(a) 0 - 200 km depth

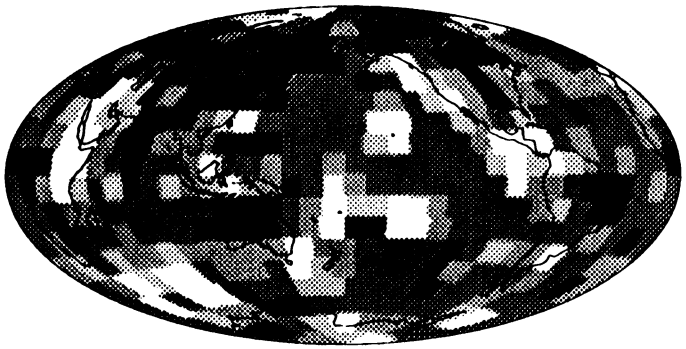

(b) 200 - 400 km depth

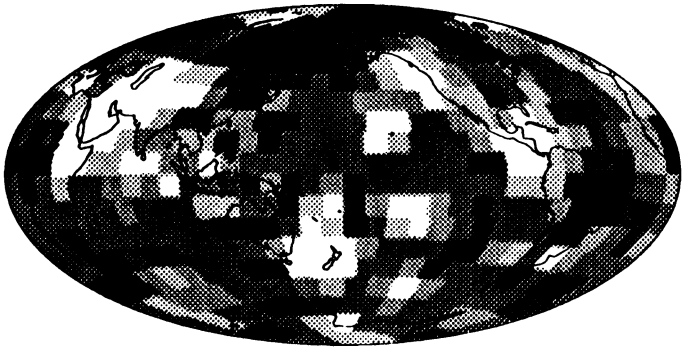

(c) 400 - 670 km depth

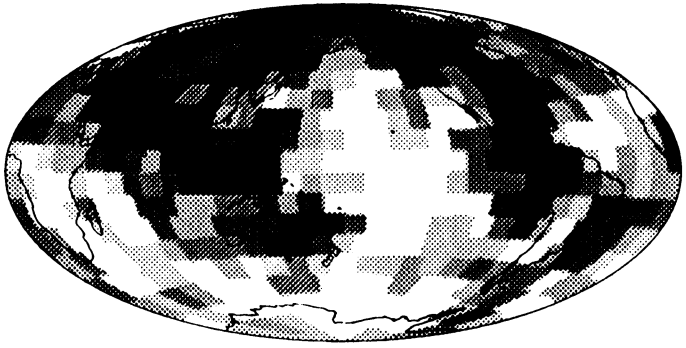

(d) 1270 - 1470 km depth

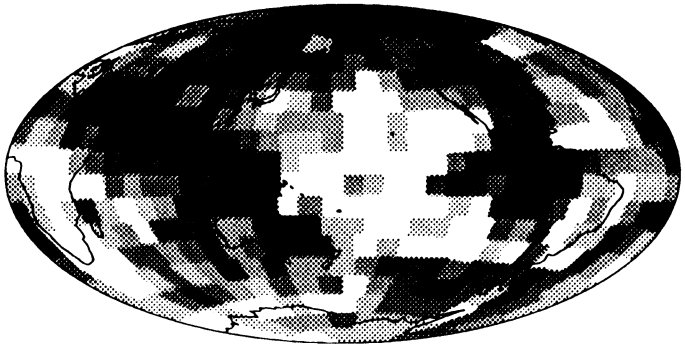

(e) 1470 - 1670 km depth

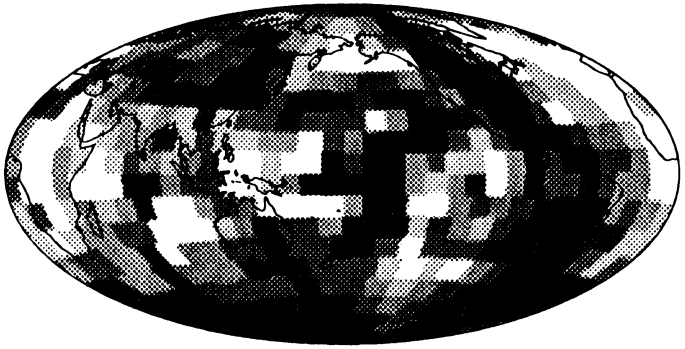

(f) 2470 - 2670 km depth

fig 11

fig 12

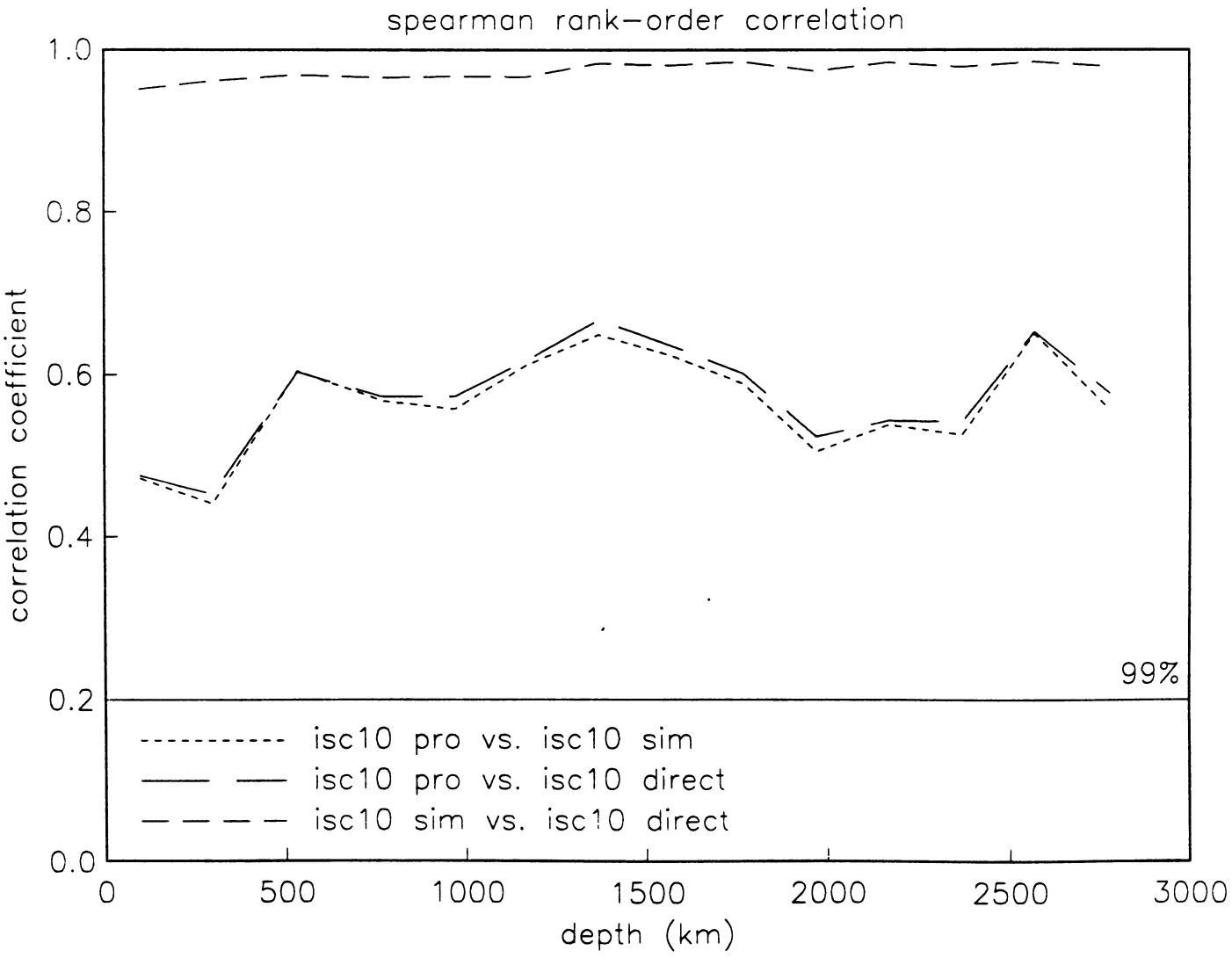
spearman rank-order correlation
1.0
0.8
0.6
0.4
0.2
0.0
correlation coefficient
99%
isc10 pro vs. isc10 sim
isc10 pro vs. isc10 direct
isc10 sim vs. isc10 direct
0
500
1000
1500
2000
2500
3000
depth (km)

Fig. 13

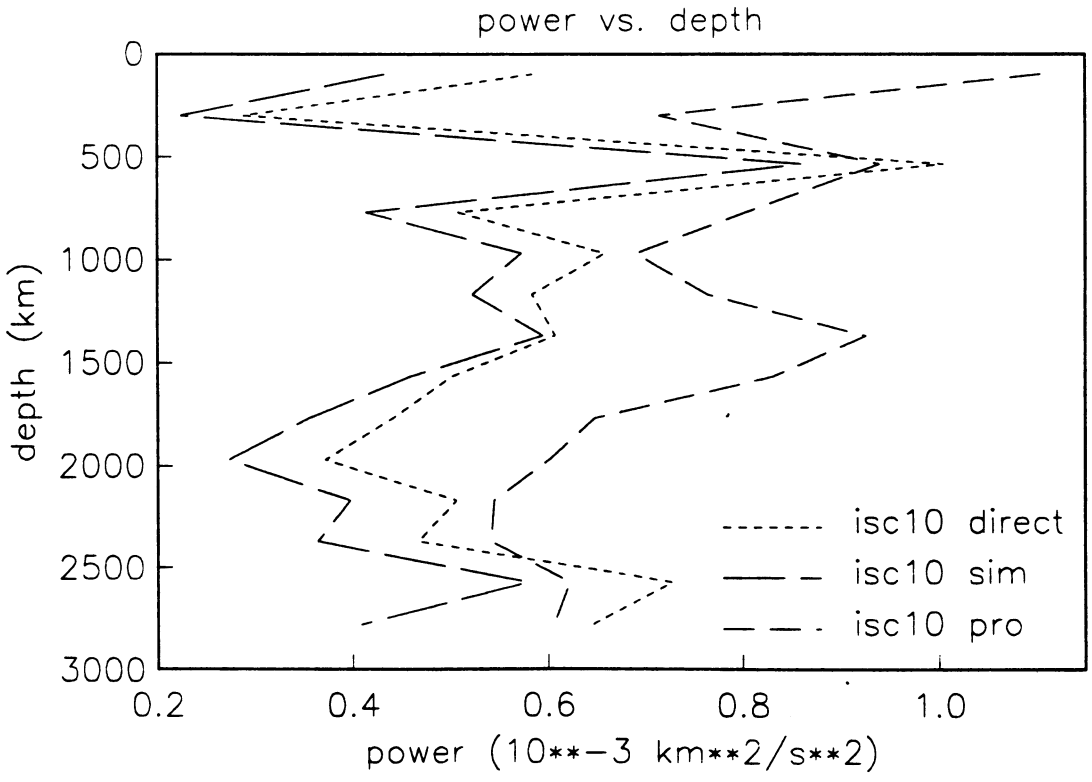
power vs. depth
0
500
1000
1500
2000
2500
3000
depth (km)
0.2
0.4
0.6
0.8
1.0
power (10**−3 km**2/s**2)
isc10 direct
isc10 sim
isc10 pro

Inversion without Source Terms

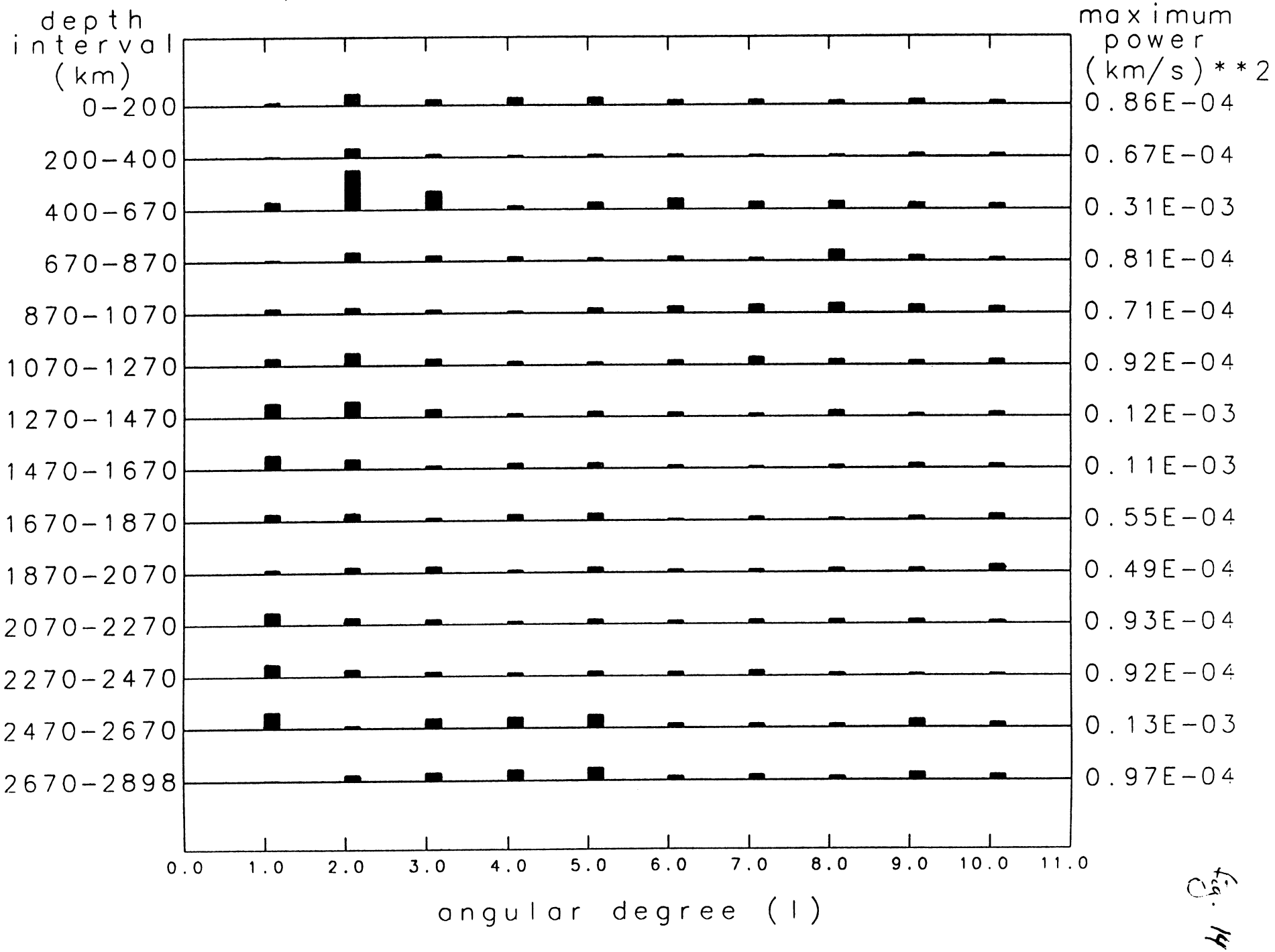

Fig. 4

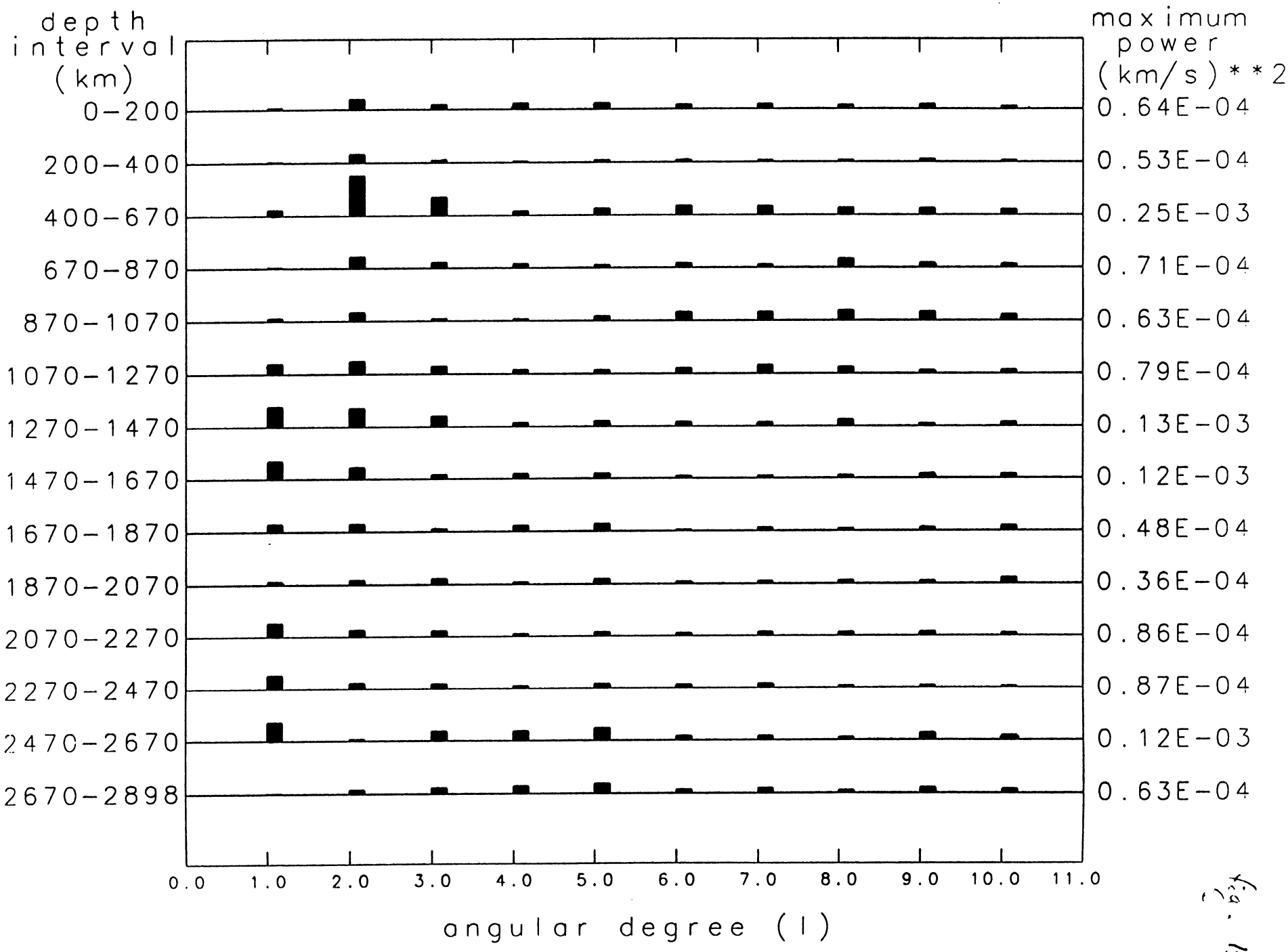
Simultaneous Inversion
depth interval (km)
maximum power (km/s)**2
0-200
0.64E-04
200-400
0.53E-04
400-670
0.25E-03
670-870
0.71E-04
870-1070
0.63E-04
1070-1270
0.79E-04
1270-1470
0.13E-03
1470-1670
0.12E-03
1670-1870
0.48E-04
1870-2070
0.36E-04
2070-2270
0.86E-04
2270-2470
0.87E-04
2470-2670
0.12E-03
2670-2898
0.63E-04
0.0
1.0
2.0
3.0
4.0
5.0
6.0
7.0
8.0
9.0
10.0
11.0
angular degree (l)

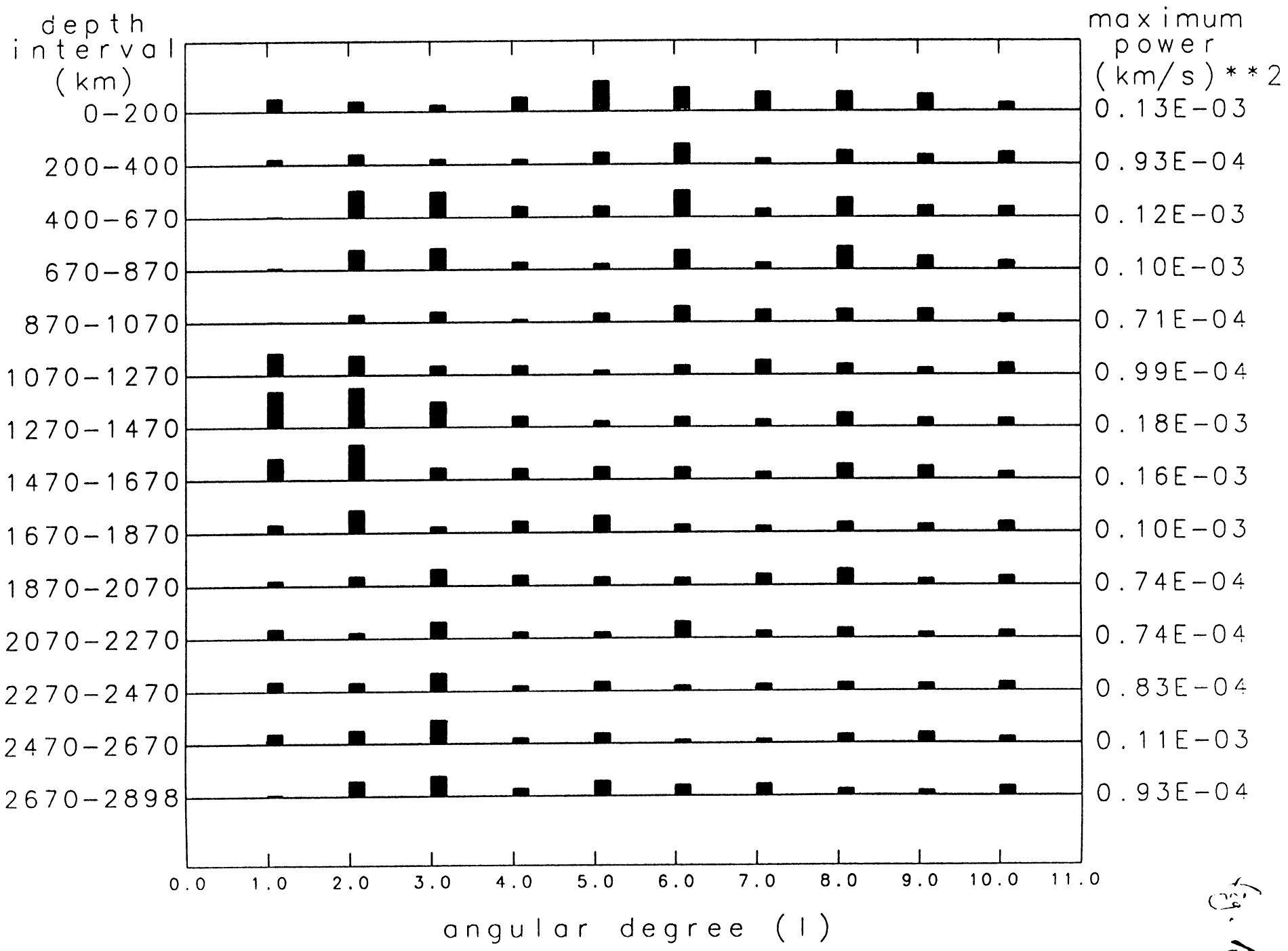
Progressive Inversion
depth interval (km)
maximum power (km/s)**2
0-200
0.13E-03
200-400
0.93E-04
400-670
0.12E-03
670-870
0.10E-03
870-1070
0.71E-04
1070-1270
0.99E-04
1270-1470
0.18E-03
1470-1670
0.16E-03
1670-1870
0.10E-03
1870-2070
0.74E-04
2070-2270
0.74E-04
2270-2470
0.83E-04
2470-2670
0.11E-03
2670-2898
0.93E-04
0.0 1.0 2.0 3.0 4.0 5.0 6.0 7.0 8.0 9.0 10.0 11.0
angular degree (l)

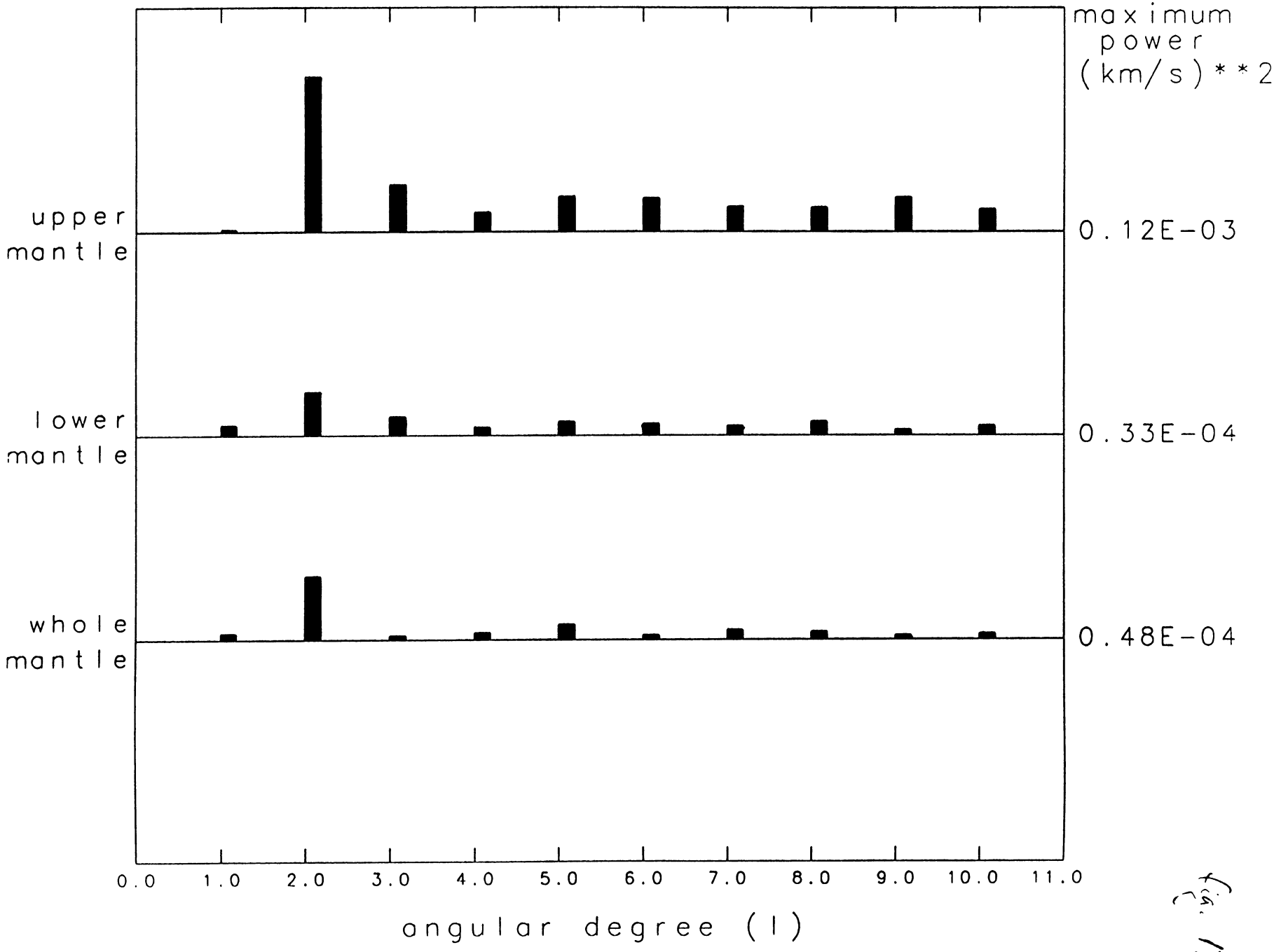
Inversion without Source Terms
averaged through the mantle
maximum
power
(km/s)**2
upper
mantle
0.12E-03
lower
mantle
0.33E-04
whole
mantle
0.48E-04
0.0
1.0
2.0
3.0
4.0
5.0
6.0
7.0
8.0
9.0
10.0
11.0
angular degree (l)

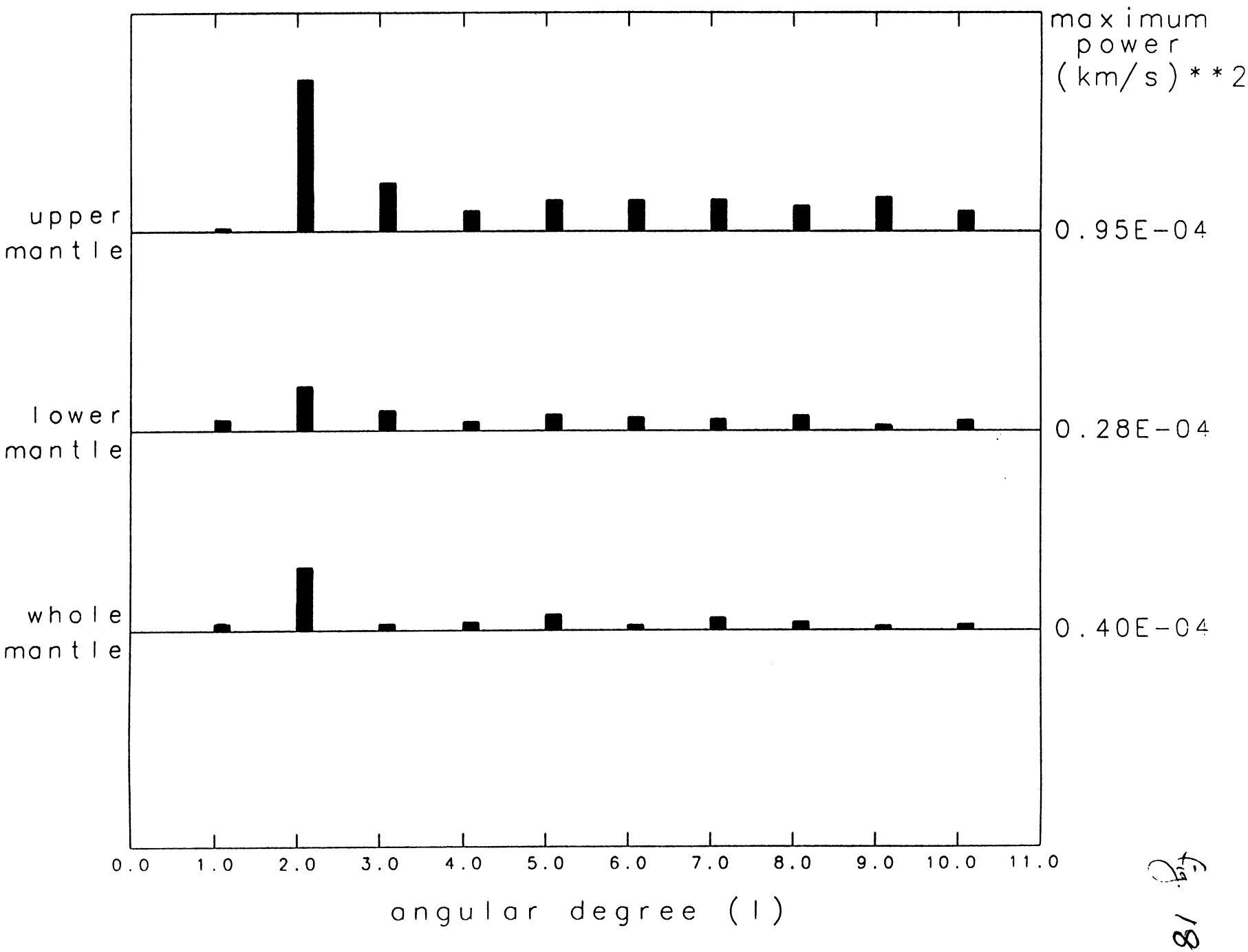
Simultaneous Inversion
averaged through the mantle
maximum
power
(km/s)**2
upper
mantle
0.95E-04
lower
mantle
0.28E-04
whole
mantle
0.40E-04
0.0
1.0
2.0
3.0
4.0
5.0
6.0
7.0
8.0
9.0
10.0
11.0
angular degree (l)

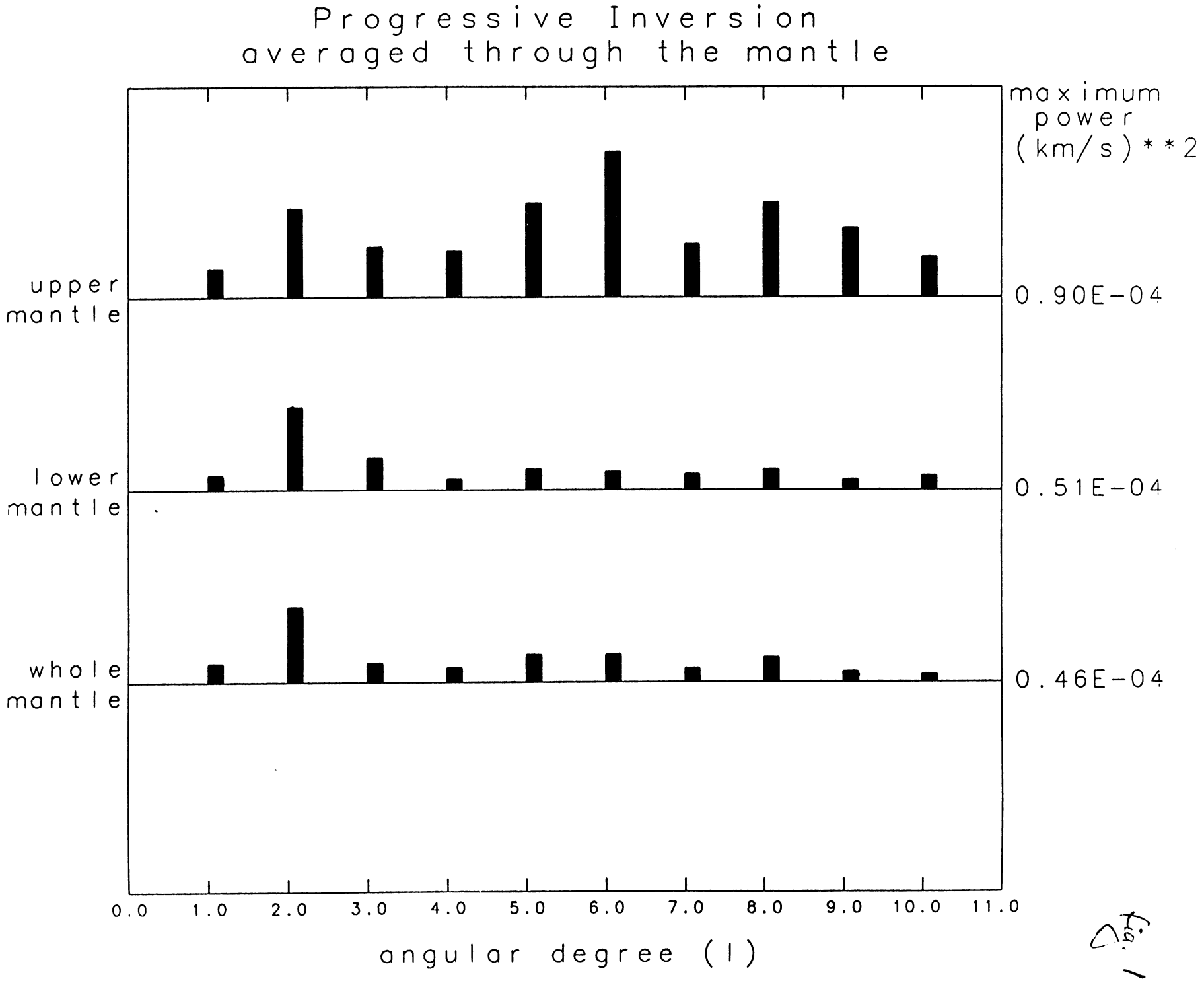
Progressive Inversion
averaged through the mantle
maximum
power
(km/s)**2
upper
mantle
0.90E-04
lower
mantle
0.51E-04
whole
mantle
0.46E-04
0.0
1.0
2.0
3.0
4.0
5.0
6.0
7.0
8.0
9.0
10.0
11.0
angular degree (l)

Fig. 14

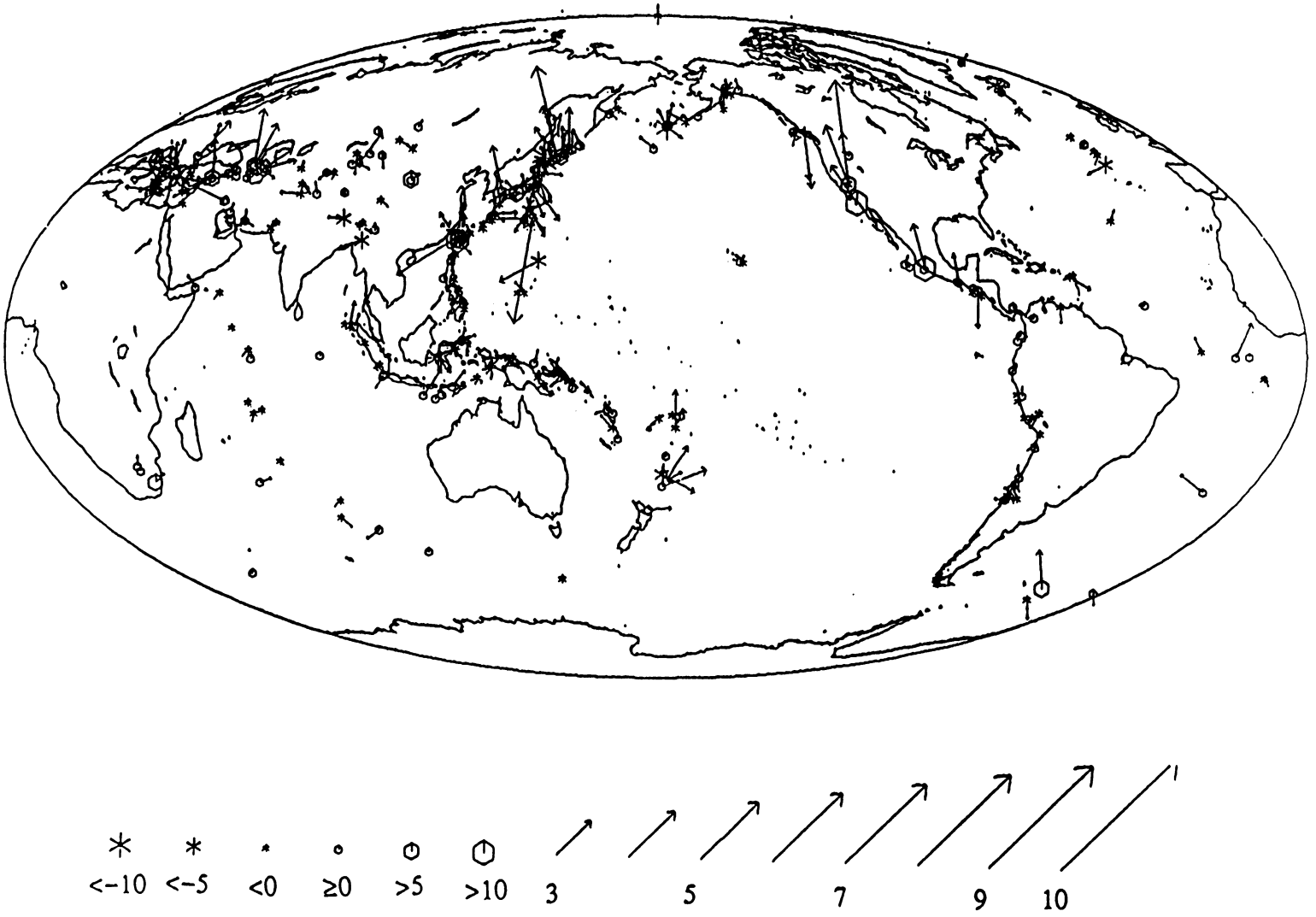
<-10
<-5
<0
≥0
>5
>10
3
5
7
9
10
δh = Δ(source depth)
source correction vector length (km)

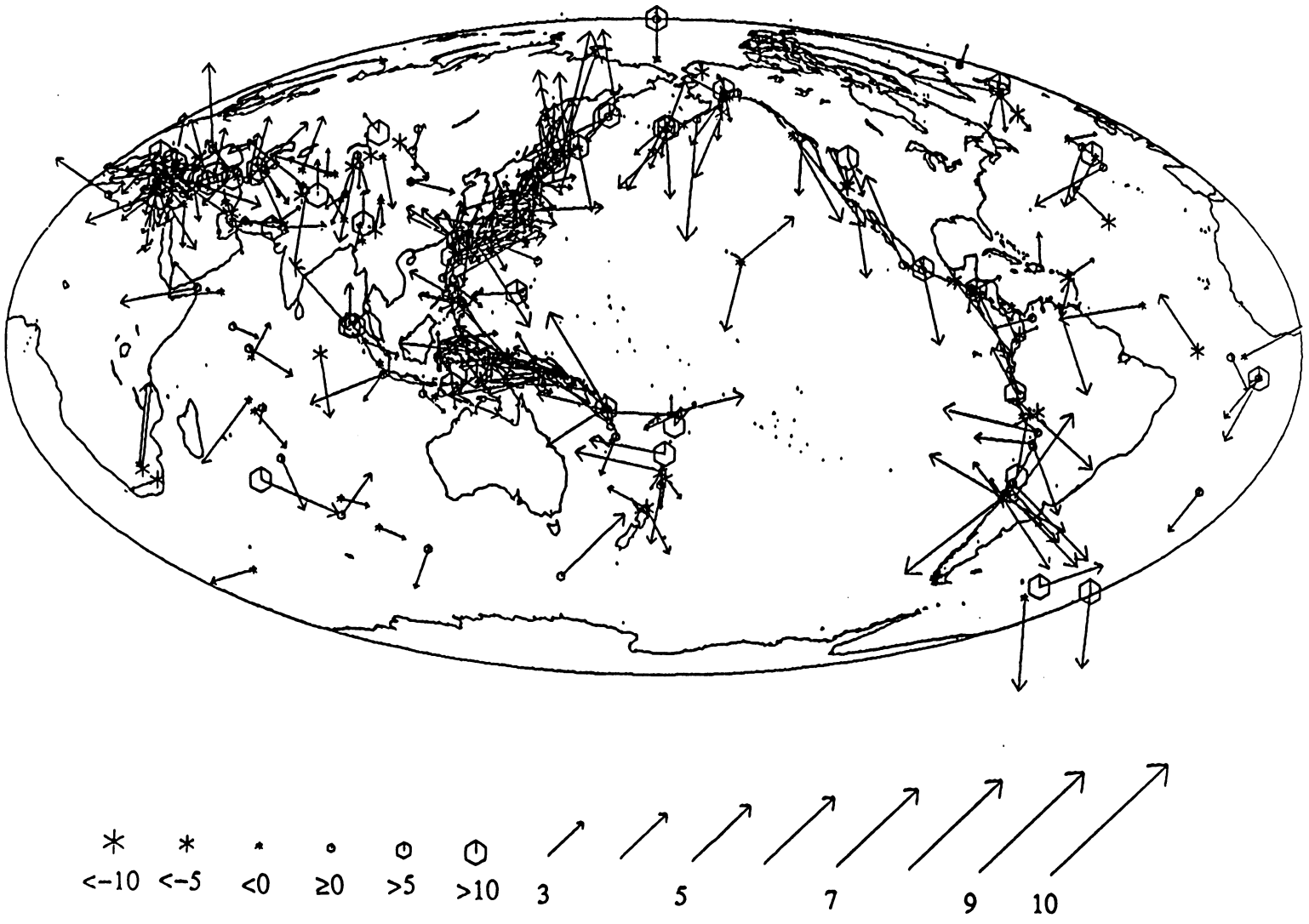
<-10
<-5
<0
≥0
>5
>10
3
5
7
9
10
δh = Δ(source depth)
source correction vector length (km)